mater.scichina.com link.springer.com

Published online 24 January 2024 | https://doi.org/10.1007/s40843-023-2755-2
Sci China Mater 2024, 67(2): 444–472

SPECIAL TOPIC: Heterojunction in Photocatalysts

g-C_3N_4-based S-scheme heterojunction photocatalysts

Xinhe Wu*, Lihong Tan, Guoqiang Chen, Jiayue Kang and Guohong Wang*

ABSTRACT With the vigorous progress of industrialization, energy shortage and environmental contamination emerge increasingly serious. Photocatalysis technology is known as a hopeful approach to resolving the above crises owing to its numerous prominent advantages and widespread applications. Among various photocatalysts, graphitic carbon nitride (g-C_3N_4) has been broadly applied in fields of fuel production and environment purification because of its unique electronic structure, extreme thermal stability, and prominent photoelectrical activity. However, single-component g-C_3N_4, similar to other photocatalysts, usually suffer from low photocatalytic efficiency due to the fact that single-constituent photocatalysts cannot synchronously equip with strong redox abilities of photogenerated charges and high light energy utilization. Fortunately, constructing Step-scheme (S-scheme) heterojunctions between g-C_3N_4 with other semiconductor photocatalysts can simultaneously overcome the typical shortcomings of low light energy utilization, rapid recombination, and weak redox abilities of carriers, thus prominently boosting its catalytic reaction rate. In view of the currently extensive reports of g-C_3N_4-based S-scheme heterojunctions, this review presents a relatively comprehensive comment on the latest research progress of the background, the proposal of conception, fundamental theory, design and preparation, characterization methods of g-C_3N_4-based S-scheme heterojunctions. Additionally, various applications of g-C_3N_4-based S-scheme heterojunctions have been detailly illustrated through example discussion and list comparison, involving photocatalytic H_2 generation, CO_2 reduction, H_2O_2 evolution, pollutant degradation, and others. Finally, the research progress and shortcomings of g-C_3N_4-based S-scheme heterojunctions are summarized, and the future research direction is prospected.

Keywords: photocatalysis, g-C_3N_4, heterojunction, S-scheme, applications

INTRODUCTION

With the vigorous progress of industrialization, energy shortage and environmental contamination emerge increasingly serious [1,2]. Photocatalysis is known as a hopeful technology to resolve the two major energy and environment crises because of its low cost, mild reaction process, and eco-friendly advantages [3–5]. In other words, photocatalysis technology refers that under the drive of solar energy, photocatalysts can trigger a series of reactions to produce fuels and repair the environment involving H_2 production, CO_2 reduction, antibiotic removal, and pollution degradation [6,7]. In the case of identical external conditions, the efficiency of photocatalysis technology is mainly depended on the photocatalysts [8,9]. Therefore, it is very necessary to develop efficient photocatalysts. Graphitic carbon nitride (g-C_3N_4), a representative of organic photocatalysts, has drawn considerable attention since its first application in H_2 evolution because of its unique electronic structure and prominent photoelectrical activity [10]. In recent years, g-C_3N_4 has been widely applied in the fields of H_2 production, CO_2 reduction, H_2O_2 production, and environment purification [11].

For the pure g-C_3N_4, similar to other single-constituent photocatalysts, usually suffers low photocatalytic efficiency owing to its low light energy utilization, rapid recombination, and weak redox abilities of photogenerated charges [12]. In this case, many strategies have been designed to overcome the above shortcomings to enhance the photocatalytic efficiency of g-C_3N_4, such as elemental doping, cocatalyst modification, and improvement of specific surface areas or crystallization degree [13,14]. However, none of the above modification strategies can simultaneously resolve the above typical shortcomings of the single photocatalyst. Namely, single-constituent photocatalysts cannot synchronously equip with strong redox abilities of photogenerated charges and high light energy utilization [15]. Additionally, the drawback of low carrier separation efficiency has always been the bottleneck hindering the improvement of photocatalysis efficiency. In view of the above-mentioned facts, constructing heterojunctions between g-C_3N_4 with another semiconductor photocatalyst can simultaneously overcome the typical shortcomings of low utilization efficiency solar energy, rapid recombination, and weak redox abilities of carriers [16], thus prominently improving the catalytic reaction of g-C_3N_4. In recent years, numerous g-C_3N_4-based heterojunctions have been constructed and aimed at enhancing the photocatalytic activity.

According to the difference in carrier transmission paths, the previously reported heterojunctions can be divided into Type-II, Z-scheme, and S-scheme, which will be briefly illustrated as follows [17]. For the Type-II heterojunction in Fig. 1a, such a carrier transfer process would not only cause the reduction of redox ability of photogenerated charges but also generate energy loss due to the repulsion between the same kind of charges [18]. To resolve the emerged deficiency in the Type-II heterojunction, a liquid Z-scheme heterojunction concept was put forward [19].

Hubei Key Laboratory of Pollutant Analysis and Reuse Technology, College of Chemistry and Chemical Engineering, Hubei Normal University, Huangshi 435002, China
* Corresponding authors (emails: wuxinhe@hbnu.edu.cn (Wu X); wanggh2003@163.com (Wang G))

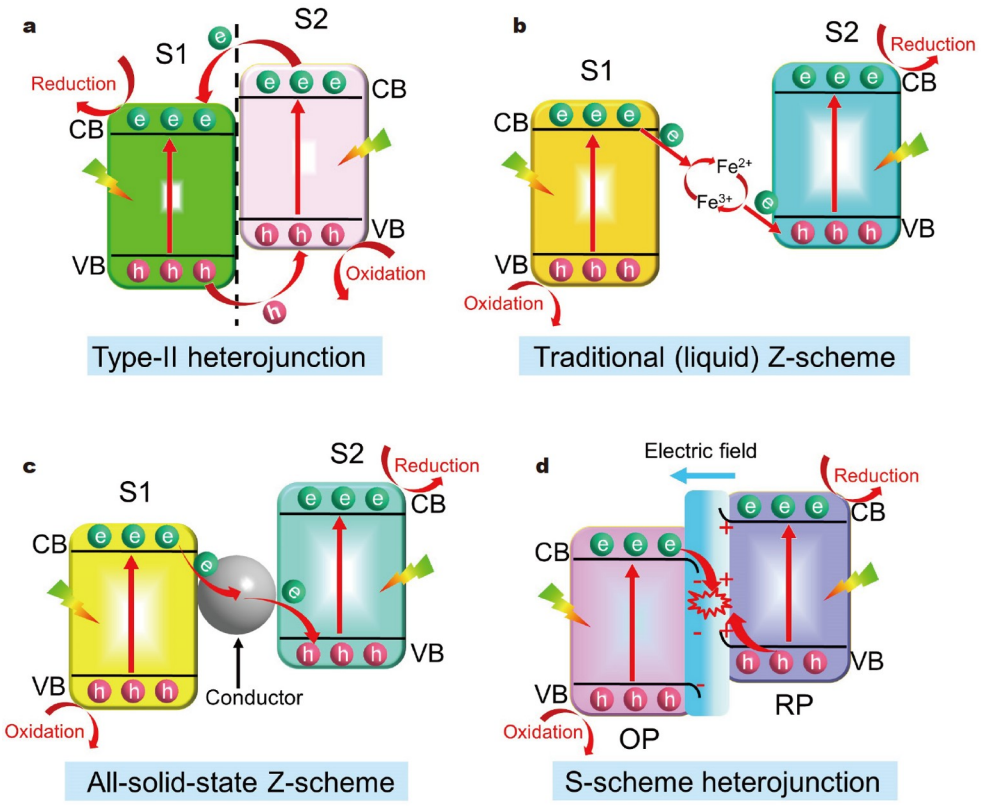

Figure 1 Possible charges migration ways for (a) Type-II, (b) liquid Z-scheme, (c) all-solid-state Z-scheme, and (d) S-scheme heterojunctions.

In contrast to the Type-II heterojunction, the obvious difference for liquid Z-scheme heterojunction is that the suitable redox couples were added and served as the charge transport channel (Fig. 1b). In fact, there is still serval irrationality in the liquid Z-scheme heterojunction. Firstly, the designed charge migration direction is not scientific because the reduction capacity of the photoinduced electrons in the Semiconductor 2 (S2) is stronger than that of Semiconductor 1 (S1), and it is much easier to reduce Fe^{3+} into Fe^{2+} (Fig. 1b). Secondly, the redox ion pairs would freely move around in the system and not be exactly fixed between the two semiconductors. Hence, an all-solid-state Z-scheme concept was proposed with solid metal conductors instead of liquid redox ion pairs (Fig. 1c) [20], which could effectively avoid the problem of random movement of ion pairs in liquid Z-scheme. However, the proposed all-solid-state Z-scheme still has the same unscientific carrier migration direction as the liquid Z-scheme. Consequently, both the Type-II and Z-scheme heterojunction systems exhibit some unscientific and illogical aspects, which would promote the birth of a fire-new scientific and rational heterojunction concept [21].

In 2019, a fire-new concept of Step-scheme (S-scheme) heterojunction was put forward by Fu *et al.* [22]. Specifically, Yu and co-workers [23,24] constructed a WO_3/g-C_3N_4 heterojunction photocatalyst and scientifically explained the reason for its significantly enhanced activity by a novel S-scheme heterojunction mechanism. Since then, S-scheme heterojunction has been extensively and deeply studied by scientific research workers all over the world. In a S-scheme system, the photoexcitation charges with powerful redox capacity are retained to be involved in interfacial catalytic reaction, while the weak ones are recombined due to the function of a built-in electric field (Fig. 1d) [25]. Therefore, constructing of S-scheme heterojunction can not only strengthen the redox ability of photoexcitation carriers but also effectively promote the separation and transmission of theirs, thus greatly boosting the catalytic reaction rates of S-scheme heterojunction systems.

In view of the above prominent advantages of the S-scheme heterojunction, such as reinforced redox ability, separation efficiency, and optical absorptivity, g-C_3N_4-based S-scheme heterojunction photocatalytic systems have been widely designed to increase the photocatalytic reaction rate of g-C_3N_4. Herein, this review presents a relatively comprehensive comment on the latest research progress of g-C_3N_4-based S-scheme heterojunctions, involving the background and proposal of conception for S-scheme heterojunction. Moreover, the fundamental theory, design, and preparation, characterization methods of g-C_3N_4-based S-scheme heterojunctions are explained by theory and examples. Then, the various applications of g-C_3N_4-based S-scheme heterojunctions have been detailly illustrated through example discussion and list comparison, including the photocatalytic H_2 evolution, CO_2 reduction, H_2O_2 production pollutant degradation, and others. Finally, the research progress and shortcomings of g-C_3N_4-based S-scheme heterojunctions are summarized, and the future research direction is prospected.

g-C_3N_4-BASED S-SCHEME HETEROJUNCTIONS

Fundamental theory

The S-scheme heterojunction charge transfer mechanism has been widely recognized and used by numerous scientists, mainly because of its rationality and scientificity, which is completely different from traditional Type II and Z-scheme heterojunctions.

In an S-scheme heterojunction system (Fig. 2a), it is generally made up of an oxidation photocatalyst (OP) and a reduction photocatalyst (RP). When the OP and RP establish contact, the free electrons on the conductive band (CB) of RP will be driven to transfer to the CB of OP by Fermi level matching balance, thereby building an interfacial electric field from RP to OP (Fig. 2b) [21]. Moreover, the energy bands of OP will bend downward at the heterogeneous interface, while the RP will reverse. Upon light irradiation, the photoexcited holes and electrons with weak redox ability on the valence band (VB) of RP and CB of OP will occur recombination owing to the attraction of interfacial electric field, while the photogenerated charges with powerful redox capacity will be retained onto the CB of RP and VB of OP by the repulsion of interfacial electric field, respectively. Finally, the charges with powerful redox capacity will take part in the following photocatalytic reaction (Fig. 2c) [26]. Consequently, the charge transmission path of S-scheme heterojunction follows the scientific principle, and its migration mechanism not only ensures efficient carrier separation but also enhances the redox capacity of the photocatalytic system.

Design and preparation

As is well known, the conduction and valence-band potentials of semiconductors are the primary parameters to be considered for designing and preparing heterojunctions. For instance, an S-scheme heterojunction system usually involves a reduction and an OP [27]. Specifically, a semiconductor with a very negative conduction potential is commonly used as an RP, while the positive one is generally served as an OP [28]. g-C_3N_4, one of the representatives of organic polymer photocatalysts, exhibits a relatively moderate band structure and small bandgap (2.7 eV), has been broadly combined with other photocatalysts to establish heterojunctions [29]. Due to its comparatively negative reduction potential, g-C_3N_4 is generally used as an RP to construct S-scheme heterojunctions with some OPs such as WO_3, TiO_2, and Fe_2O_3 in Fig. 3 [30]. Additionally, g-C_3N_4 is also combined with some more reductive semiconductors (such as $CuInS_2$ and ZnCoS) to form S-scheme heterojunctions, where g-C_3N_4 acts as the OP [31]. Consequently, g-C_3N_4-based S-scheme heterojunctions have been abundantly established due to the prominent electronic structure and photoelectrical properties of g-C_3N_4.

According to the above design regulations, varieties of preparation methods have been explored to synthesize g-C_3N_4-based S-scheme heterojunctions, such as electrostatic self-assembly, hydrothermal, high-temperature calcination, vapour deposition, solvothermal, and thermal polymerization methods [30]. For instance, Fu *et al.* [22] constructed a two-dimensiaonal (2D)/2D WO_3/g-C_3N_4 heterojunction by an electrostatic self-assembly strategy (Fig. 4a), which involves the initial exfoliation of bulk g-C_3N_4 and WO_3 into nanosheet structure and the following surface treatment making them with positive and negative charges, respectively, resulting in the final combination of WO_3 and g-C_3N_4 nanosheets *via* Coulomb attraction. Moreover, correlation test reports suggested that the WO_3/g-C_3N_4 heterojunction formed by Coulomb force attraction had good contact, high stability, and significantly enhanced photocatalytic activity,

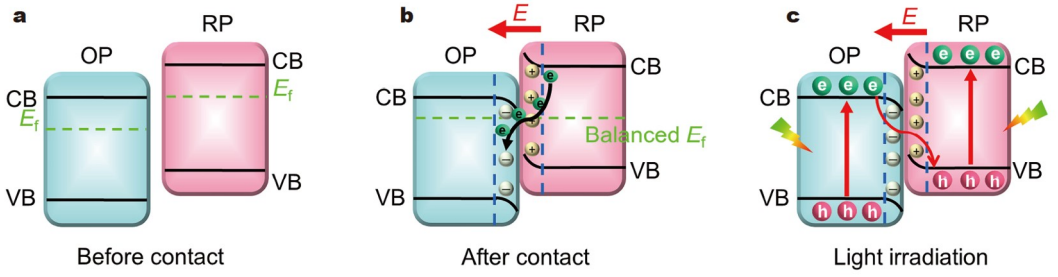

Figure 2 Fundamental theory of carrier-transfer for S-scheme heterojunction.

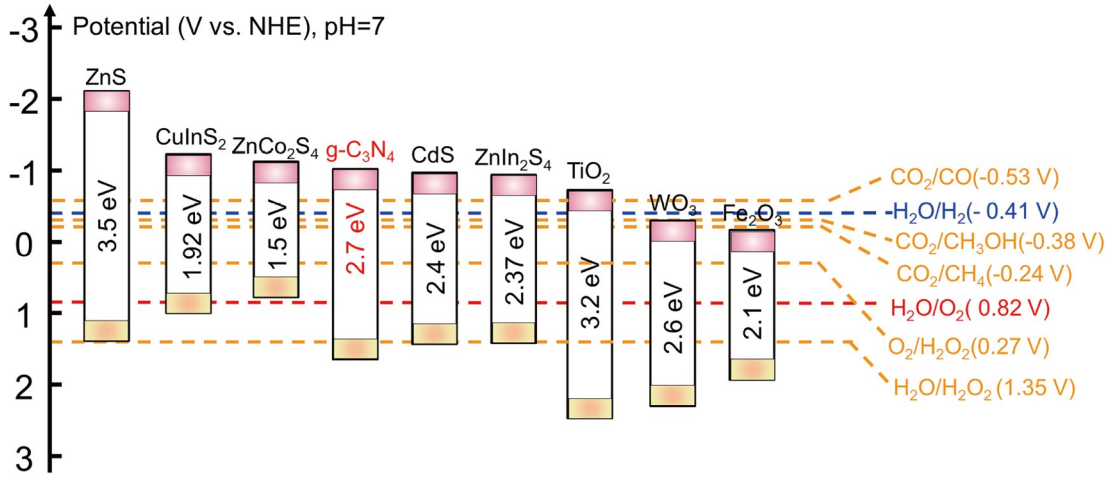

Figure 3 Band gaps and positions of some representative photocatalysts.

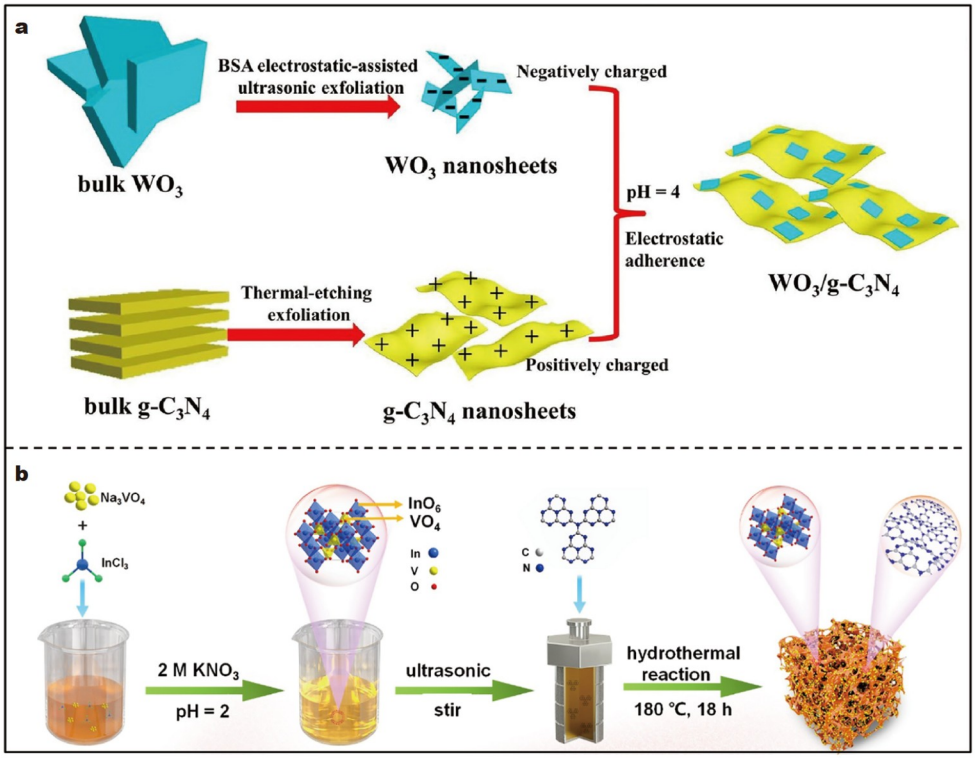

Figure 4 Graphic illustration of (a) WO_3/g-C_3N_4 heterojunctions by an electrostatic self-assembly strategy. Reprinted with permission from Ref. [22]. Copyright 2019, Elsevier. (b) $InVO_4$/g-C_3N_4 heterojunctions *via* a hydrothermal method. Reprinted with permission from Ref. [32]. Copyright 2021, Elsevier.

and its carrier migration mode followed the S-scheme heterojunction mechanism. Additionally, Gong *et al.* [32] fabricated a $InVO_4$/g-C_3N_4 heterojunction *via* a facile hydrothermal method, including primarily premixing the raw materials formed $InVO_4$ and subsequently mixing with g-C_3N_4, finally undergoing a hydrothermal treatment (Fig. 4). In fact, during the finally hydrothermal treatment, $InVO_4$ was *in-situ* generated onto the g-C_3N_4 surface to form the $InVO_4$/g-C_3N_4 S-scheme heterojunction. Similarly, the resulting $InVO_4$/g-C_3N_4 S-scheme heterojunction also possessed well-contact heterojunction interfaces and prominent photocatalytic activities. On the whole, most g-C_3N_4-based S-scheme heterojunctions produced by the currently reported methods have good contact and stability because of the unique interface structure and thermal polycondensation of g-C_3N_4.

Characterization method

Until now, a variety of advanced characterization techniques have been developed to investigate the charge transfer path of g-C_3N_4-based S-scheme heterojunctions, such as *in-situ* irradiated X-ray photoelectron spectroscopy (ISIXPS), density functional theory (DFT) calculation, electron paramagnetic resonance (EPR), femtosecond transient absorption spectroscopy (FT-AS), and Kelvin probe force microscopy (KPFM) [33,34]. In the above characterization techniques, the ISIXPS and EPR spectra were widely applied to verify the carrier transmission mechanism of S-scheme heterojunction [35], which will be successively introduced by the examples below.

XPS is a progressive technique that can accurately measure the chemical shift and binding energy. Generally, for a specific semiconductor, if it receives electrons, the corresponding binding energy will shift toward higher potential; on the contrary, the binding energy will conversely shift [36]. For example, Qaraah and co-workers [37] scientifically revealed the S-scheme heterojunction charge migration mechanism between O-doped g-C_3N_4 (OCN) and N-doped Nb_2O_5 (NNBO) by an ISIXPS characterization. As presented in Fig. 5, compared with the pure NNBO, the binding energy of Nb 3d and O 1s for the OCNNb composite (without light irradiation) exhibited a shift towards lower binding energy (Fig. 5a, b), while the corresponding binding energy changes of N 1s and C 1s were opposite (Fig. 5c, d). The above changes could be mainly because when OCN and NNBO came into contact (formed heterojunction), the free electrons in OCN would transfer to the NNBO owing to their different Fermi levels, which would cause accumulations of electrons and holes onto the NNBO and OCN sides, respectively, thus generating a built-in electric field orientation from OCN to NNBO. Under light irradiation, the binding energy of Nb 3d and O 1s for the OCNNb composite exhibited a shift towards higher binding energy, whereas the corresponding changes for OCN were reversal, which primarily because under the influence of built-in electric field, the photogenerated electrons on NNBO would migrate to the OCN and occur recombination with the holes (Fig. 5e), thus retaining the carriers with powerful redox capacity to involve in interfacial catalytic reaction. Consequently, the above ISIXPS results accurately and comprehensively demonstrated that the charge migration path between NNBO and OCN obeyed S-scheme heterojunction rather than Type-II heterojunction.

Additionally, EPR spectra have also been broadly applied to reveal the carrier transmission mechanism of g-C_3N_4-based S-scheme heterojunctions. For example, Fu *et al.* [22] properly

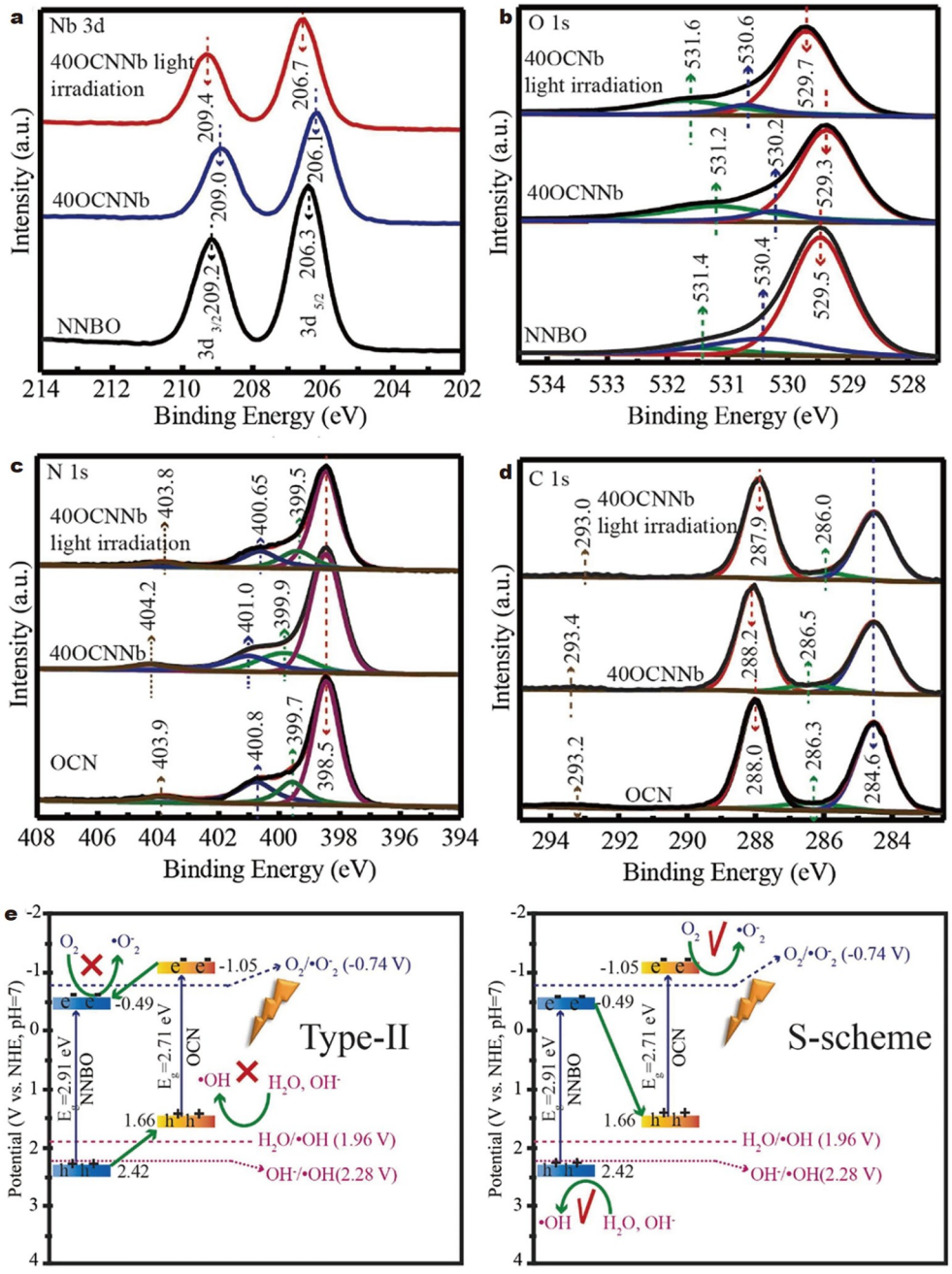

Figure 5 High-resolution XPS spectra of (a) Nb 3d, (b) O 1s, (c) N 1s, and (d) C 1s. (e) Mechanism inference and analysis. Reprinted with permission from Ref. [37]. Copyright 2022, Elsevier.

revealed that the carrier transfer path between WO_3 and g-C_3N_4 followed S-scheme mechanism *via* EPR spectra, as exhibited in Fig. 6. Evidently, the DMPO-·OH signals were sensitively captured in pure WO_3 and WO_3/g-C_3N_4 composites, while that could not be observed for pure g-C_3N_4 (Fig. 6a), mainly indicating that photogenerated holes tended to stay on the VB of WO_3 and did not migrate to the VB of g-C_3N_4. Simultaneously, the DMPO-·O_2^- signals could be clearly observed in pure g-C_3N_4 and WO_3/g-C_3N_4 composites, whereas a much weaker signal could be detected from pure WO_3 (Fig. 6b), suggesting that photoinduced electrons on g-C_3N_4 possessed enough reducing capacity to reduce O_2 to ·O_2^- and did not transmit to the CB of WO_3. As a consequence, the photoinduced carriers with powerful redox capacity tended to remain on the VB of WO_3 and CB of g-C_3N_4, respectively. In other words, the carrier transmission path between WO_3 and g-C_3N_4 followed the S-scheme heterojunction mechanism (Fig. 6c) rather than Type-II heterojunctions.

In addition to the above ISIXPS and EPR characterization means, KPFM, DFT calculations, and FT-AS spectrum can also afford strong data to investigate the charge migration mechanism of g-C_3N_4-based S-scheme heterojunctions [38]. For example, KPFM can receive the variations of heterojunction surface potential with and without illumination, thus judging the carrier migration mode; FT-AS can detect the differences in absorption spectra between single components and complexes to deduce the

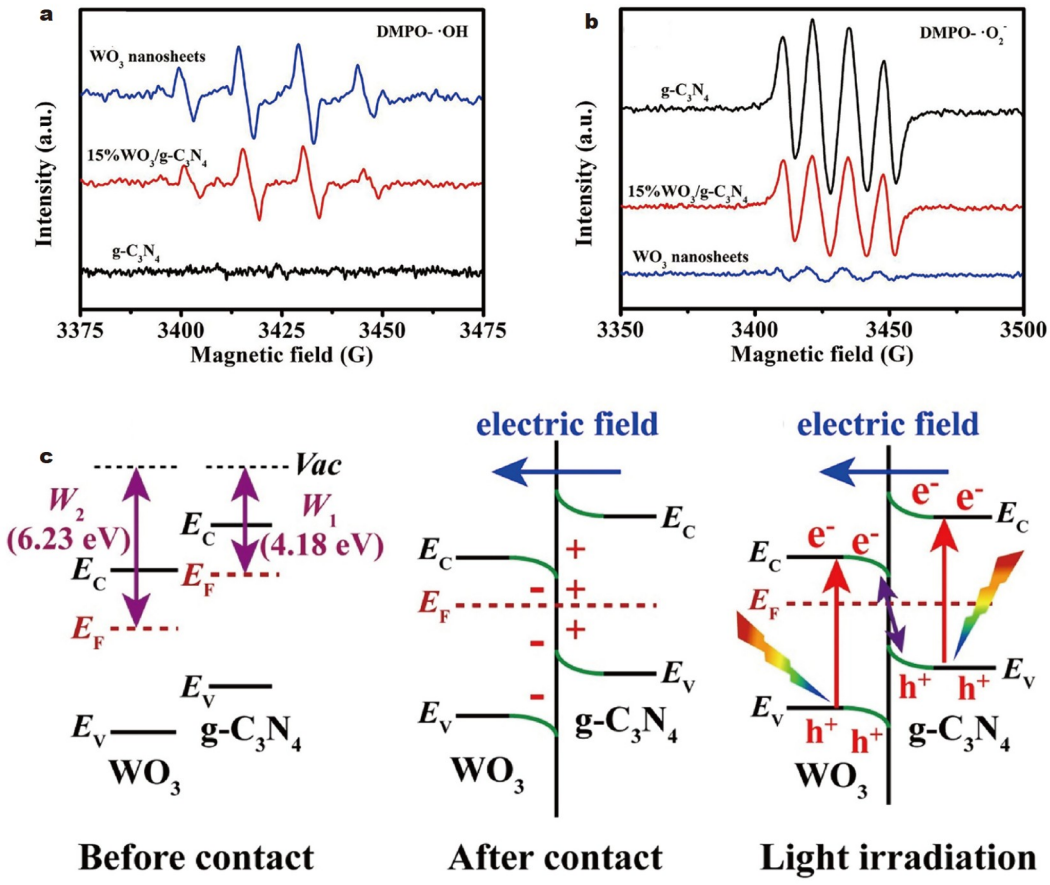

Figure 6 EPR signals of (a) DMPO-·OH and (b) DMPO-·O_2^-. (c) Charge migration mechanism. Reprinted with permission from Ref. [22]. Copyright 2019, Elsevier.

carrier migration mechanism. In general, the above-advanced characterizations can provide sufficient and powerful evidence for the S-scheme heterojunction carrier transmission mechanism. Furthermore, more advanced characterizations need to be exploited to demonstrate the S-scheme heterojunction mechanism.

APPLICATIONS

Nowadays, g-C_3N_4-based S-scheme heterojunction photocatalytic systems have been abundantly constructed and used in numerous fields because of their effective charge transmission and strong redox capability [39]. The previous reports on g-C_3N_4-based S-scheme heterojunctions are mainly concentrated in the field of energy and environment involving H_2 production, CO_2 reduction, H_2O_2 production, and pollutant degradation [30].

H_2 evolution

Hydrogen (H_2) energy is a secondary clean energy, with high combustion value, green and clean, zero emissions, and other advantages, known as the "ultimate energy in the 21st century", but also in the context of carbon peak and carbon neutral, need to accelerate the exploitation of clean energy. Among many new technologies, photocatalytic H_2 generation refers that photocatalysts can split water into H_2 under the drive of solar energy [40]. g-C_3N_4 has been a star material in the field of hydrogen production in the past decade due to its prominent photoelectric property and suitable band structure [41]. However, the severe recombination and limited reduction ability of carriers for single-component g-C_3N_4 lead to its weak H_2 production performance. Among a variety of modification methods, the construction of g-C_3N_4-based S-scheme heterojunctions can prominently reinforce the separation efficiency and redox capacity of carriers, thus significantly enhancing their photocatalytic activity.

Due to the relatively negative reduction potential, g-C_3N_4 is usually coupled with some oxidizing semiconductors to construct S-scheme heterojunctions, such as metal oxides, oxysalts, and organic polymers [30]. For example, Li *et al.* [42] fabricated a C/O doped g-C_3N_4 (COCN)/$W_{18}O_{49}$ heterojunction by an *in-situ* solvothermal method. During the solvothermal process, the nanowire-like $W_{18}O_{49}$ would form and *in-situ* generate onto the COCN nanosheet surface (Fig. 7a). Transmission electron microscope (TEM) images of COCN/$W_{18}O_{49}$ heterojunction clearly presented a typically translucent and flaky structure with several nanowire-like structures lying flat on its surfaces (Fig. 7b, c), visually proving the formation of COCN nanosheet/$W_{18}O_{49}$ nanowire heterojunction. The as-prepared COCN/$W_{18}O_{49}$ heterojunction displayed a prominent H_2 production rate of ca. 3908.2 μmol h^{-1} g^{-1} under simulated sunlight, which is nearly 12 times higher than that of conventional g-C_3N_4 (Fig. 7d). To reveal the mechanism of performance enhancement, the EPR spectra were carried out in Fig. 7e, f. The DMPO-·O_2^- signals were obviously detected in COCN and COCN/

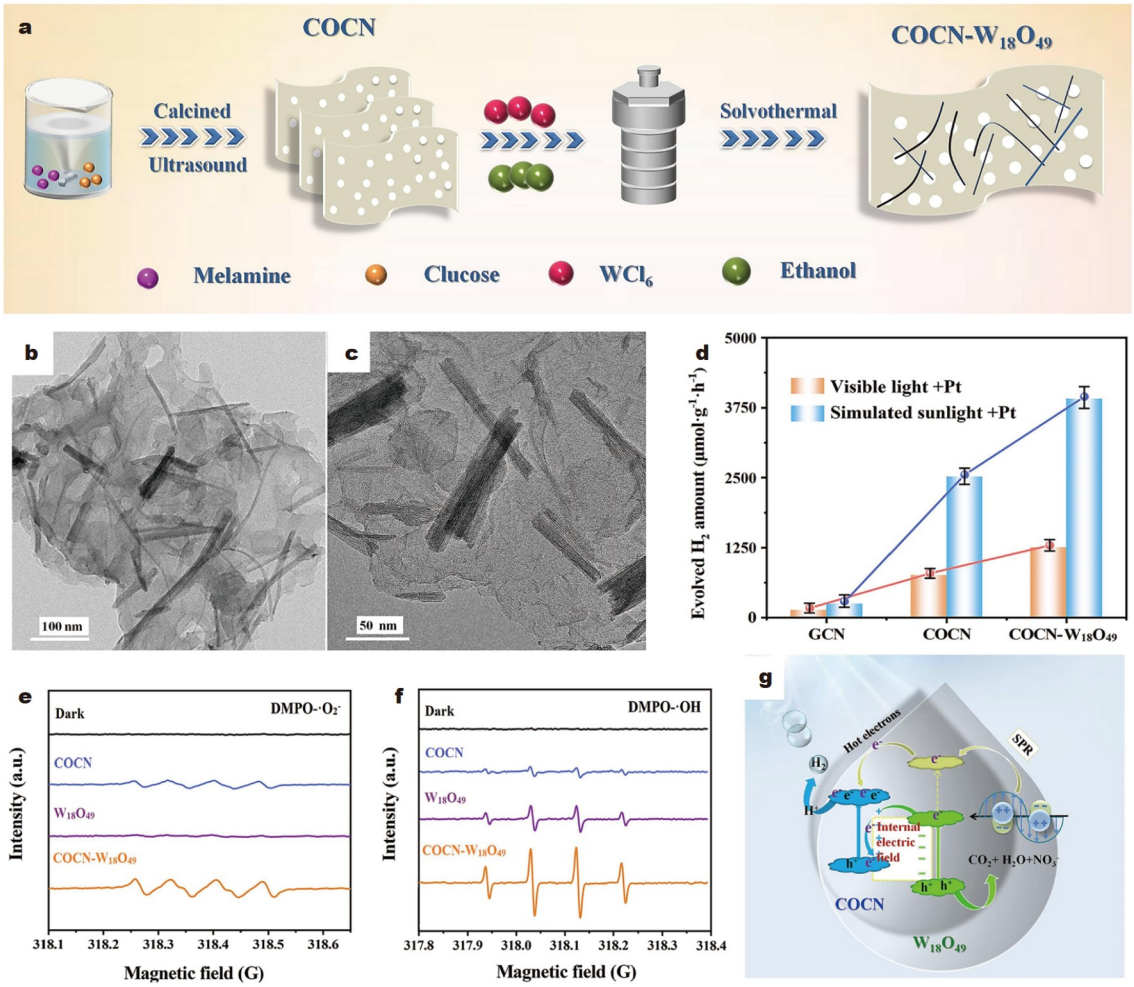

Figure 7 (a) Synthetic process and (b, c) TEM images of COCN-$W_{18}O_{49}$ heterojunction. (d) H_2 evolution rates, (e, f) EPR spectra, and (g) photocatalytic mechanism in COCN-$W_{18}O_{49}$ heterojunction. Reprinted with permission from Ref. [42]. Copyright 2023, Elsevier.

$W_{18}O_{49}$ samples, while that could not be detected from $W_{18}O_{49}$ (Fig. 7e), powerfully indicating that photoinduced electrons of COCN possessed enough reducing capacity to reduce O_2 to $\cdot O_2^-$ and did not transfer to the CB of $W_{18}O_{49}$. However, the DMPO-·OH signals were reversed (Fig. 7f), owing to that photoinduced holes tended to stay on the VB of $W_{18}O_{49}$. Evidently, the EPR results directly demonstrated that the carrier transmission path obeyed the S-scheme mechanism (Fig. 7g), which cooperated with the SPR effect to synergistically promote the enhancement of H_2-production performance.

In addition to the above combinations with oxidizing photocatalysts, g-C_3N_4 occasionally served as an oxidized semiconductor to design S-scheme heterojunctions with some metal sulfides. For example, Shi *et al.* [43] constructed a cobalt phthalocyanine/oxygen-doped g-C_3N_4 (CoPc/OCN) heterojunction photocatalyst *via* an ultrasonic method. It was found that CoPc particles were dispersedly loaded on the surface of g-C_3N_4 nanosheets (Fig. 8a). Moreover, the heterojunction interface between CoPc and OCN could be clearly observed from their HRTEM image in Fig. 8b. Additionally, the optimized H_2-evolution rate of the resultant CoPc/OCN heterojunction reached 9560 μmol h^{-1} g^{-1}, over 2.6-fold superior to the pure g-C_3N_4 (Fig. 8c). To investigate the charge transfer route of CoPc/OCN heterojunction, the KPFM potential images and their corresponding surface potential curves were supplied in Fig. 8d–f. In the dark, the surface potential of CoPc was larger than that of OCN. However, with light irradiation, the surface potential of CoPc emerged an obvious decrease, while that of OCN increased, indicating that the photoinduced electrons tended to stay on the CoPc, while the photoinduced holes stayed on the OCN. Apparently, the above KPFM results strongly suggested that the carrier transfer way between CoPc and OCN followed S-scheme heterojunction (Fig. 8g). Therefore, the greatly enhanced activity of CoPc/OCN principally profited from their generated S-scheme heterojunction.

According to the above reports and S-scheme heterojunction mechanism, it is not difficult to conclude that the interfacial electric field is the key factor driving the transmission of photoexcitation charges in S-scheme heterojunctions. Therefore, it is extremely indispensable to investigate the relationship between heterojunction electric field intensity and its corresponding photocatalytic activity. For this purpose, Zhu *et al.* [44] adopted nonmetal doping to regulate the interfacial electric field intensity of g-C_3N_4/SnS_2 and g-C_3N_4/ZrS_2 S-scheme heterojunctions and investigated the structure-activity relationship between the electric field intensity and photocatalytic activity. Specifically, compared with pristine g-C_3N_4, when oxygen atoms were doped into g-C_3N_4, the work function of resultant O-C_3N_4 would

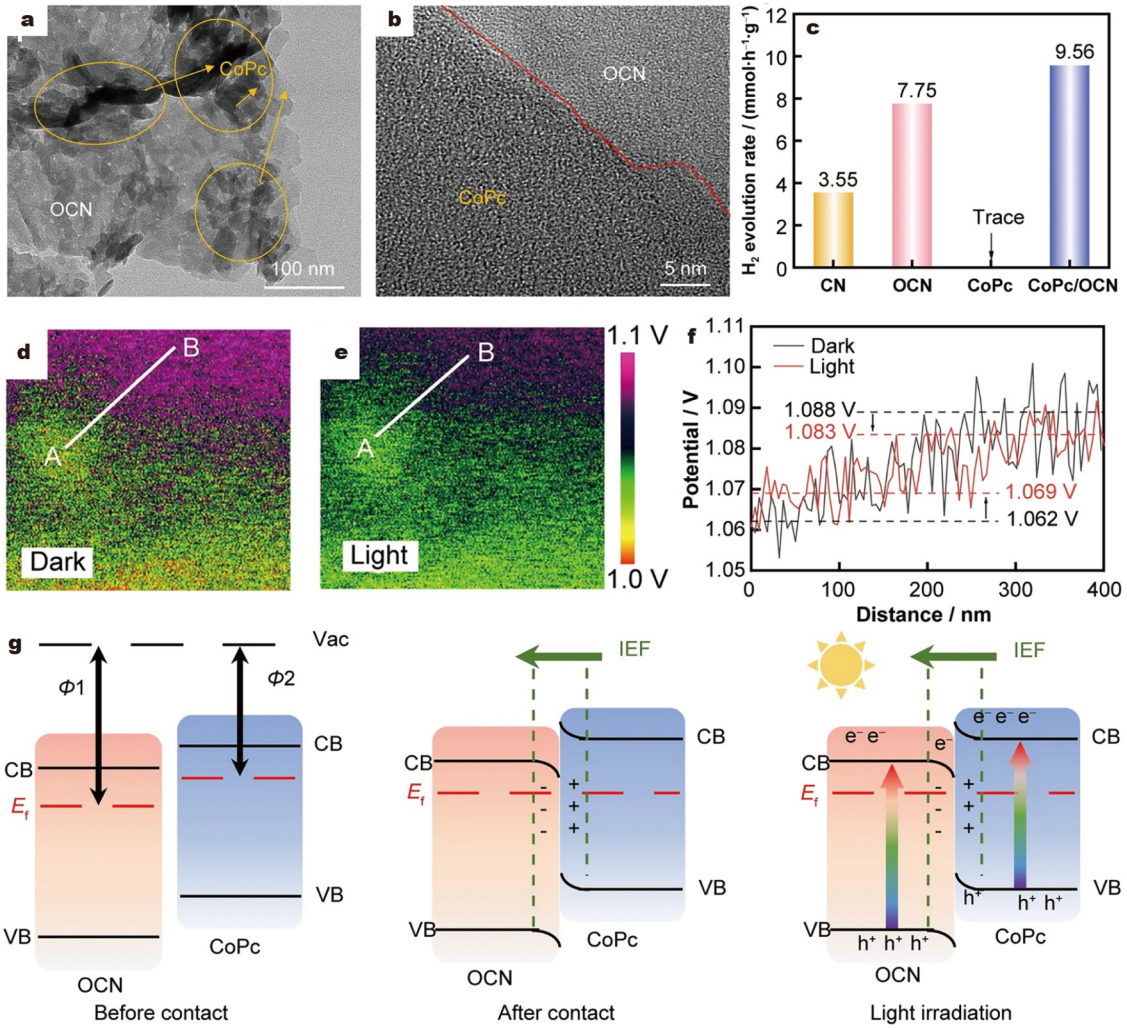

Figure 8 (a, b) TEM images of CoPc/OCN. (c) H_2 evolution rates. (d, e) KPEM images and (f) the corresponding surface potential curves. (g) Photocatalytic charge migration mechanism. Reprinted with permission from Ref. [43]. Copyright 2023, Springer.

decrease (Fermi energy level would shift up) (Fig. 9a), which would increase the Fermi energy level difference between C_3N_4 and SnS_2, resulting in an obviously increased in the number of transferred charges (Fig. 9a), thus increasing the intensity of the interface electric field (Fig. 9b, c). Moreover, the electric field strengths of g-C_3N_4 doped with other elements (P, S) were also calculated when constructing heterojunction with SnS_2 and ZrS_2, as exhibited in Fig. 9d. Apparently, the electric field intensities of oxygen-doped g-C_3N_4 when forming heterojunction with other semiconductors were much higher than that of pristine g-C_3N_4, P-doped g-C_3N_4, and S-doped g-C_3N_4. Finally, experimental validation results indicated that the H_2-evolution rate of O-C_3N_4/SnS_2 heterojunction (154 μmol h^{-1} g^{-1}) was significantly higher than that of g-C_3N_4/SnS_2 heterojunction (38 μmol h^{-1} g^{-1}), which was consistent with the calculated results of electric field strength in Fig. 9d. Consequently, enhancing the interfacial electric field intensity of S-scheme heterojunction is an effective strategy to further enhance its photocatalytic activity, which provides a new direction for the subsequent construction of S-scheme heterojunctions.

Additionally, the most recently reported S-scheme g-C_3N_4-based heterojunction systems for H_2 production have been displayed in Table 1 [22,42–84]. On the whole, all the constructed g-C_3N_4-based S-scheme heterojunctions presented highly improved photocatalytic H_2 production performance, even some of the works have achieved an order of magnitude improvement for hydrogen production. For example, Hafeez *et al.* [45] prepared a rGO/$NiFe_2O_4$-g-C_3N_4 S-scheme heterojunction to achieve efficient hydrogen production. The as-prepared rGO/$NiFe_2O_4$-g-C_3N_4 heterojunction showed an extremely prominent photocatalytic hydrogen-production rate of ca. 11,817 μmol h^{-1} g^{-1}, over 70 times higher than that of the g-C_3N_4 nanosheets, which was mainly owing to the fact that the formation of S-scheme heterojunction between $NiFe_2O_4$ and g-C_3N_4 could significantly accelerate charge transmission and reinforce its redox power. Moreover, the rGO/$NiFe_2O_4$-g-C_3N_4 was magnetic, which could be easily recovered and reused. Hassan *et al.* [46] fabricated a novel V_2O_5/N-deficient g-C_3N_4 S-scheme heterojunction photocatalyst by ultrasonic treatment and high-temperature calcination. The as-fabricated V_2O_5/N-deficient g-C_3N_4 exhibited a prominent H_2 production rate of ca. 5892 μmol h^{-1} g^{-1}, which was over 13-fold superior to the g-C_3N_4. The enhanced performance could be principally attributed to the fact that the fabricated S-scheme heterojunction

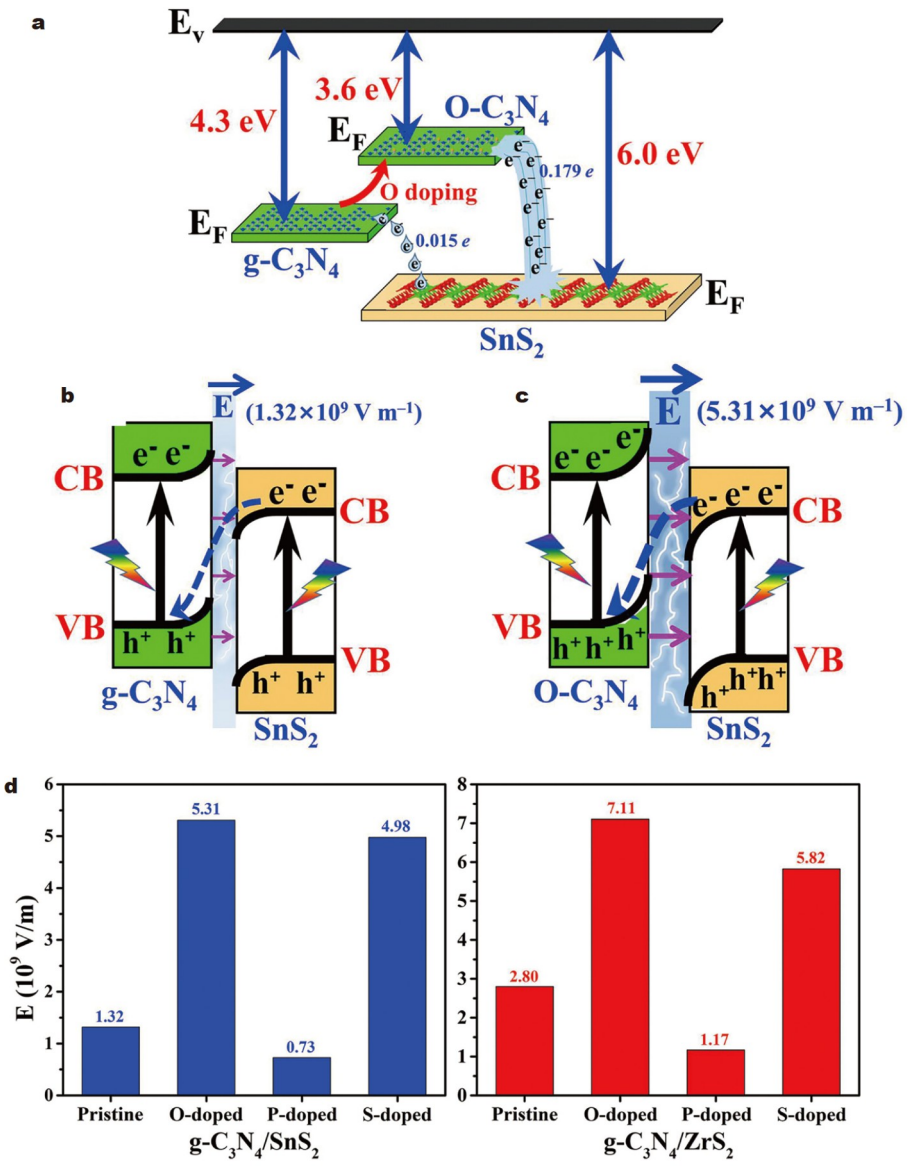

Figure 9 (a) Electron migration under different Fermi levels. Photocatalytic mechanisms of (b) g-C_3N_4/SnS_2 and (c) O-C_3N_4/SnS_2 heterojunction. (d) Strength of interfacial electric field (IEF) in g-C_3N_4/MS_2 heterojunctions. Reprinted with permission from Ref. [44]. Copyright 2021, Elsevier.

could reinforce the carrier transmission and light absorption.

CO_2 reduction

In order to cope with the great threat to the living environment posed by rapid global climate change, developing effective CO_2 removal technologies to achieve a balanced CO_2 content in the atmosphere is desperately needed. Of all the new CO_2 removal technologies, photocatalytic CO_2 reduction can use the solar drive to reduce CO_2 into CO, CH_3OH, CH_4, and other valuable fuels, which can not only effectively remove the CO_2 but also reduce CO_2 into valuable fuels, concurrently solving the energy and environmental crises [85]. Compared with photocatalytic H_2 production, photocatalytic CO_2 reduction requires a photocatalyst with a stronger reducing capacity. In this case, g-C_3N_4 has been widely investigated for photocatalytic CO_2 reduction due to its strong reducing ability, visible-light reaction, and prominent photochemical property [30]. Usually, single-constituent g-C_3N_4 always suffers from serious recombination of photogenerated carriers, restricted light absorption, and redox capacity, causing its weak CO_2 reduction activity. In this case, a large number of researchers solve the above defects of single g-C_3N_4 by constructing S-scheme heterojunction, so as to effectively reinforce the photocatalytic CO_2 reduction performance of g-C_3N_4.

For instance, Wang *et al.* [86] successfully constructed a TiO_2/g-C_3N_4 nanowire array heterojunction *via* an interesting vapour deposition method. During the vapour deposition process, the generated g-C_3N_4 thin film would *in-situ* produce onto the surface of TiO_2 nanowire array (Fig. 10a). The as-constructed TiO_2/g-C_3N_4 heterojunction displayed an excellent CO_2 reduction rate of ca. 785.3 μmol h^{-1} g^{-1}, about 5.9 times superior to the g-C_3N_4 photocatalyst (Fig. 10b). To reveal the above performance enhancement mechanism, ISIXPS spectra were performed to demonstrate the carrier transmission route between TiO_2 and g-C_3N_4. As exhibited in Fig. 10c–f, compared to the pure g-C_3N_4, the binding energy of C 1s and N 1s for TiO_2/

Table 1 Recently reported g-C_3N_4-based S-scheme heterojunctions for H_2 production

S-scheme heterojunction	Cocatalyst (wt%)	Light source (wavelength/nm)	H_2 production rate (μmol h^{-1} g^{-1})	Enhancement factor *versus* g-C_3N_4	Apparent quantum yield (%)	Ref.
WO_3/g-C_3N_4	Pt (2 wt%)	350 W Xe lamp	982	1.7	–	[22]
g-C_3N_4/$W_{18}O_{49}$	Pt (*x* wt%)	Simulated solar light	3908.2	11.9	13.3	[42]
CoPc/OCN	Pt (1 wt%)	300 W Xe lamp	9560	2.7	6.9	[43]
O-C_3N_4/SnS_2	Pt (*x* wt%)	350 W Xe lamp ($\lambda \geq 420$ nm)	154	4.1	–	[44]
rGO/$NiFe_2O_4$-g-C_3N_4	–	Solar light	11,817	76	–	[45]
V_2O_5/g-C_3N_4	Pt (5 wt%)	300 W Xe lamp ($\lambda > 420$ nm)	5892	13.1	6.5	[46]
$CuInS_2$/g-C_3N_4	–	350 W Xe lamp ($\lambda > 350$ nm)	102.4	48.1	–	[47]
Ce-TiO_2/GO/g-C_3N_4	Pt (*x* wt%)	300 W Xe lamp	3050	38.7	–	[48]
$MnCo_2S_4$/g-C_3N_4	–	300 W Xe lamp	2979	26.4	0.8	[49]
WO_3/g-C_3N_4	Pt (2 wt%)	300 W Xe lamp	2971	–	13.1	[50]
$Bi_xY_{1-x}VO_4$/g-C_3N_4	Pt (1 wt%)	Xe lamp	–	–	–	[51]
$In_{2.77}S_4$/NiS_2/g-C_3N_4	–	300 W Xe lamp ($\lambda > 390$ nm)	7481.7	52.5	0.3	[52]
$NiTiO_3$/g-C_3N_4	Pt (*x* wt%)	2×250 W Tungsten-halogen lamp	576	1.4	–	[53]
AgI/g-C_3N_4	Pt (0.6 wt%)	Xe lamp ($\lambda \geq 420$ nm)	4562	10.6	3.2	[54]
In_2S_3/g-C_3N_4/CoZnAl-LDH	–	300 W Xe lamp	50.6	–	–	[55]
Co_3O_4/g-C_3N_4	–	300 W Xe lamp	105.1	41	0.05	[56]
Co-Sn_3O_4/g-C_3N_4	Pt (3 wt%)	300 W Xe lamp ($\lambda > 420$ nm)	1793.9	1.6	–	[57]
TiO_2/g-C_3N_4	Pt (1 wt%)	4 × LED[a] lamp ($\lambda = 420$ nm)	3211	7.5	1.6	[58]
g-C_3N_4/$BiO_{1.2}I_{0.6}$	–	500 W Xe lamp ($\lambda > 420$ nm)	1402.7	3.5	11.8	[59]
S-g-C_3N_4/g-C_3N_4	Pt (3 wt%)	300 W Xe lamp ($\lambda \geq 420$ nm)	5548.1	60.8	0.4	[60]
$Mn_{0.2}Cd_{0.8}$S-D/g-C_3N_4	Pt (*x* wt%)	300 W Xe lamp ($\lambda > 420$ nm)	11,420	30	–	[61]
Bi_3TaO_7/g-C_3N_4	Pt (1 wt%)	300 W Xe lamp ($\lambda > 420$ nm)	4891	3	4.1	[62]
$Ni_{0.85}Se$/g-C_3N_4	–	300 W Xe lamp	8780.3	92.9	–	[63]
$MnWO_4$/g-C_3N_4	Pt (0.5 wt%)	200 W Xe lamp	871.4	3.7	16.5	[64]
$NiTe_2$/g-C_3N_4	Pt (1 wt%)	300 W Xe lamp	2540.4	23.4	–	[65]
TiO_2-OV/g-C_3N_4	Pt (1.2 wt%)	300 W Xe lamp ($\lambda > 400$ nm)	1096	10.9	–	[66]
g-C_3N_4/CdSe-D	Pt (*x* wt%)	300 W Xe lamp ($\lambda > 420$ nm)	18,800	1446	38.4	[67]
Cu_2O/g-C_3N_4	–	500 W Xe lamp ($\lambda > 400$ nm)	480.6	4.6	–	[69]
g-C_3N_4/CdS	Pt (3 wt%)	300 W Xe lamp	3370	3.8	–	[70]
$SbVO_4$/g-C_3N_4	–	300 W Xe lamp	752	4.1	–	[71]
Ni-Sn_3O_4/g-C_3N_4	Pt (3 wt%)	300 W Xe lamp ($\lambda > 420$ nm)	1961	1.4	–	[72]
$Mn_{0.5}Cd_{0.5}Se$/g-C_3N_4	–	280 W Xe lamp	5908.3	126.6	–	[73]
Ni_2P/g-C_3N_4/$Cd_{0.5}Zn_{0.5}$Se-D	Pt (1 wt%)	300 W Xe lamp ($\lambda \geq 420$ nm)	12,627	–	37.7	[74]
N-MoS_2/S-g-C_3N_4	–	300 W Xe lamp	658.5	23	–	[75]
S-g-C_3N_4/$WO_{2.72}$	–	300 W Xe lamp ($\lambda > 420$ nm)	786	–	7.6	[76]
CdS/g-C_3N_4	–	300 W Xe lamp	15,300	3060	6.9	[77]
CdS/g-C_3N_4-GA	–	300 W Xe lamp ($\lambda > 420$ nm)	86.4	3.5	–	[78]
g-C_3N_4/CdS-DETA	Pt (0.6 wt%)	300 W Xe lamp ($\lambda > 400$ nm)	9738	12.2	10.2	[79]
MCN/UCN	Pt (1 wt%)	300 W Xe lamp ($\lambda > 420$ nm)	598	–	1.1	[80]
$W_{18}O_{49}$/g-C_3N_4	Pt (3 wt%)	300 W Xe lamp ($\lambda > 420$ nm)	4670	15.1	9.8	[81]
ZnCdS/DBTCN	Pt (1 wt%)	300 W Xe lamp	8870	6.6	14.9	[82]
$NiCo_2O_4$/g-C_3N_4	Pt (0.5 wt%)	300 W Xe lamp	424	4.2	–	[83]
Bi_2MoO_6 SOVs/g-C_3N_4	–	300 W Xe lamp ($\lambda \geq 420$ nm)	2290	12.1	–	[84]

a) LED: light-emitting diode.

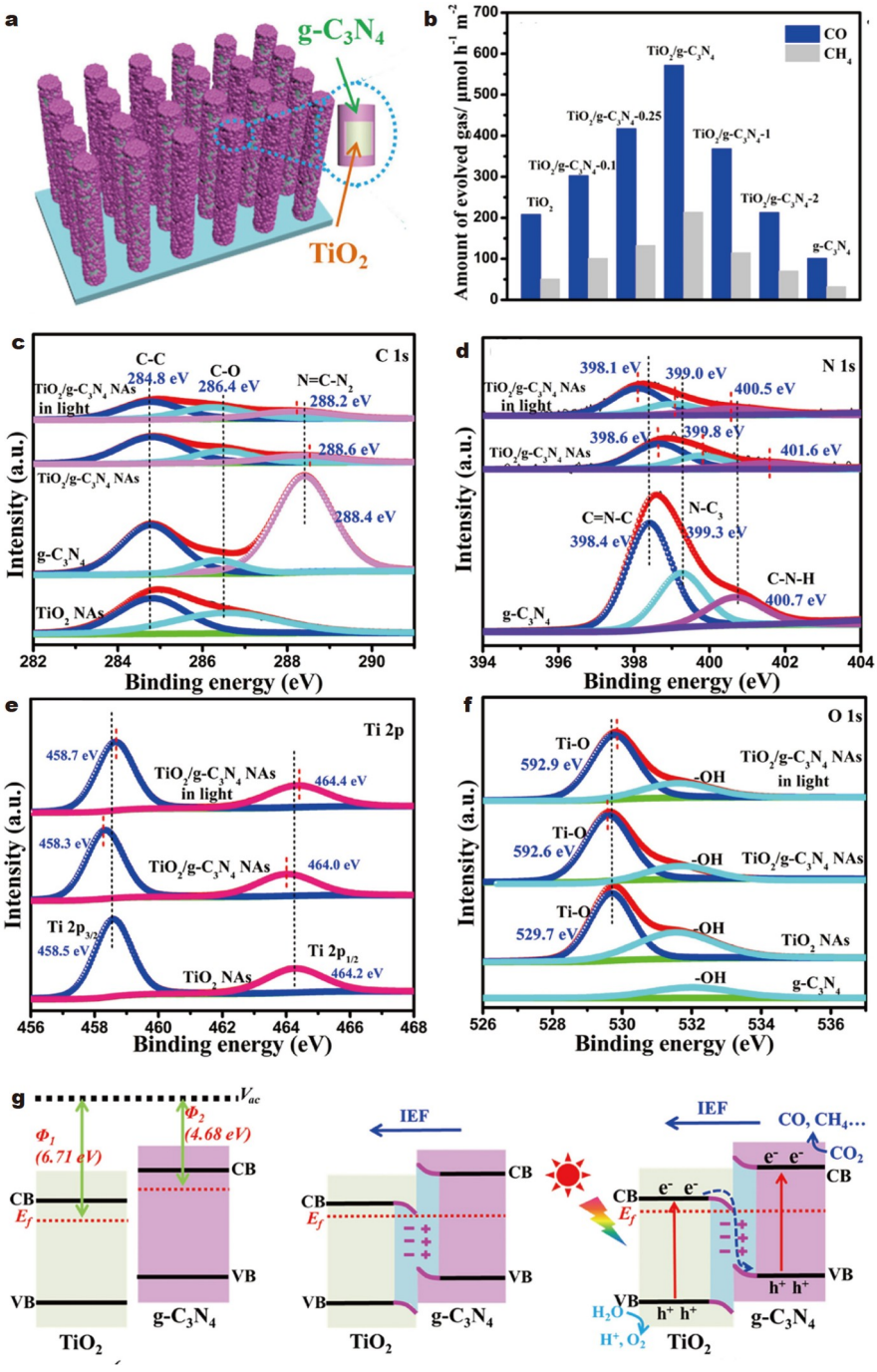

Figure 10 (a) Structure diagram of TiO_2/g-C_3N_4 heterojunction. (b) CO_2 reduction activity. (c–f) *In-situ* XPS spectra and (g) graphic illustration for the S-scheme mechanism of TiO_2/g-C_3N_4. Reprinted with permission from Ref. [86]. Copyright 2022, Elsevier.

g-C_3N_4 heterojunction (without light irradiation) exhibited a shift towards higher binding energy (Fig. 10c, d), while the corresponding binding energy changes of Ti 2p and O 1s were opposite (Fig. 10e, f). The above shifts mainly because when TiO_2 and g-C_3N_4 came into contact (formed heterojunction), the free electrons in g-C_3N_4 would transfer to the TiO_2 because of their different work function, which would cause accumulations of electrons and holes onto the TiO_2 and g-C_3N_4 sides, respectively, thus generating a built-in electric field orientation from g-C_3N_4 to TiO_2 (Fig. 10g). Under light irradiation, the binding energy of C 1s and N 1s for the TiO_2/g-C_3N_4 composite exhibited a shift towards higher binding energy, whereas the corresponding changes for TiO_2 were reversal, primarily because that with the action of a built-in electric field, the photogenerated electrons on TiO_2 would migrate to the g-C_3N_4 and occur recombination with the holes (Fig. 10g), thus retaining the carriers with powerful redox capacity to involve in interfacial catalytic reaction. Therefore, the generated TiO_2/g-C_3N_4 S-scheme heterojunction greatly contributed to their reinforced catalytic activity.

Apart from TiO_2, g-C_3N_4 is also formed S-scheme heterojunctions with other oxides. For example, Dai *et al.* [87] pre-

pared a Cu plasmonic-modified g-C_3N_4/Cu_2O S-scheme heterojunction photocatalyst by a two-step procedure, involving the initial wet chemistry process and the following in-situ chemical reduction. The g-C_3N_4, Cu_2O, and Cu could be clearly identified from the TEM and high resolution TEM (HRTEM) images of g-C_3N_4/Cu_2O@Cu composite (Fig. 11a–c). Moreover, the as-obtained g-C_3N_4/Cu_2O@Cu sample emerged with a prominent CO_2 reduction rate of about 18.9 μmol h^{-1} g^{-1}, which was obviously higher than that of pure g-C_3N_4 and Cu_2O (Fig. 11d), respectively. To disclose the charge transfer way, the EPR spectra were conducted, and the results were presented in Fig. 11e. Evidently, the DMPO-·O_2^- signals could be easily tested for the pure g-C_3N_4 and g-C_3N_4/Cu_2O@Cu composites, whereas a much weaker signal could be detected from pure Cu_2O, indicating that photoinduced electrons on g-C_3N_4 possessed enough reducing capacity and did not transport to the CB of Cu_2O. Namely, the charge transfer path between Cu_2O and g-C_3N_4 followed S-scheme heterojunction mechanism (Fig. 11f) rather than Type-II heterojunctions. Consequently, the above significantly enhanced CO_2 reduction activity could be mainly due to the synergistic promotion effects of the plasma resonance effect of Cu and the formed g-C_3N_4/Cu_2O S-scheme heterojunction (Fig. 11f).

In addition to the above combinations with oxidizing photocatalysts, g-C_3N_4 occasionally served as an oxidized semiconductor to construct S-scheme heterojunctions with some

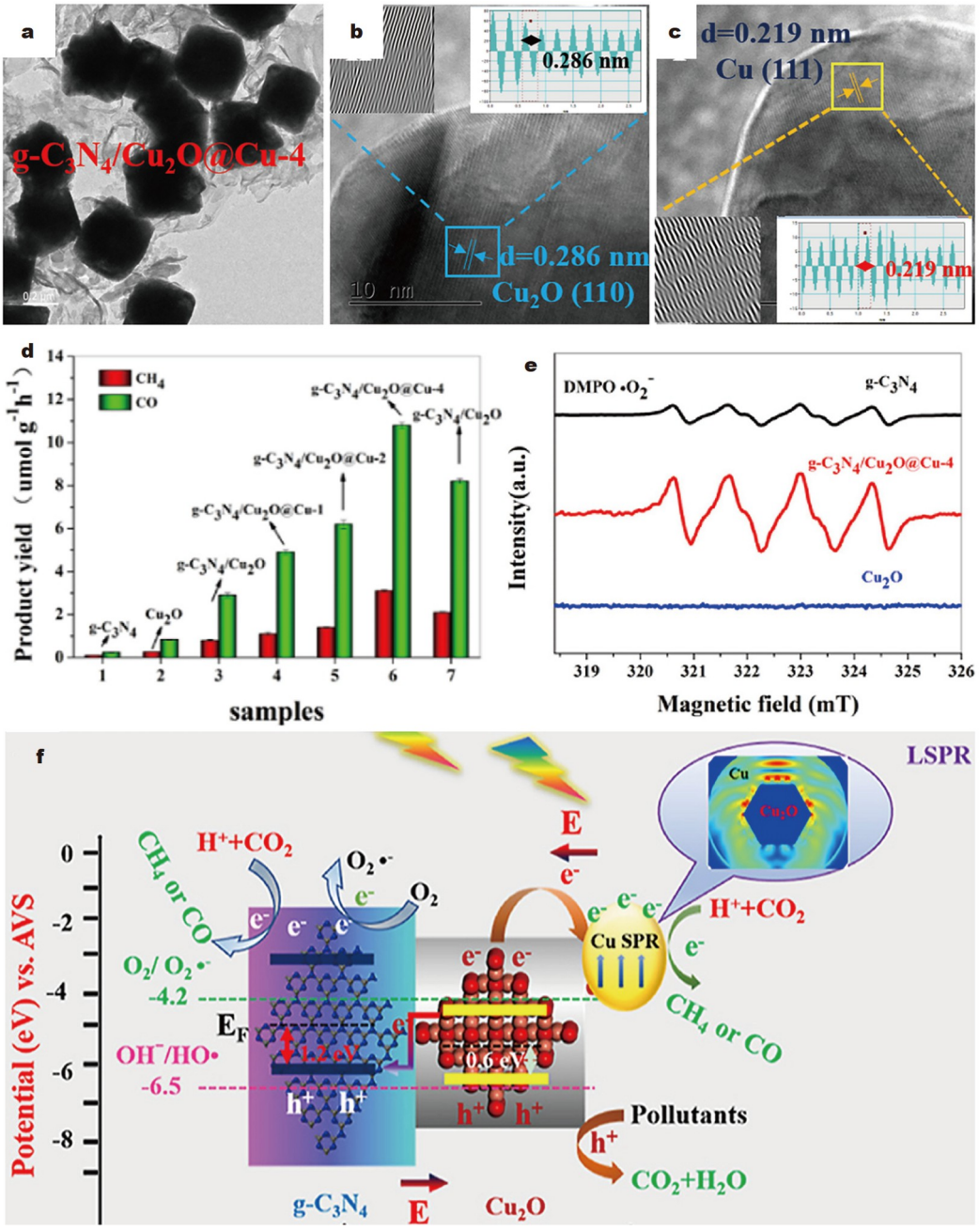

Figure 11 (a) TEM and (b, c) HRTEM images of g-C_3N_4/Cu_2O@Cu. (d) CO_2 reduction activity. (e) EPR spectra and (f) photocatalytic mechanism. Reprinted with permission from Ref. [87]. Copyright 2022, Elsevier.

metal sulfides. For instance, Lee and co-workers [88] designed a S-doped $Cu_3P/g\text{-}C_3N_4$ S-scheme heterojunction through a facile liquid-phase mixing method. Apparently, the Cu_3P emerged as an ultra-small nanoparticle structure with a size of less than 10 nm and attached to $g\text{-}C_3N_4$ surface (Fig. 12a). Moreover, the as-prepared $Cu_3P/g\text{-}C_3N_4$ composite showed an evidently enhanced CO_2 reduction rate of around 137 μmol h^{-1} g^{-1}, which is nine times superior to the pure $g\text{-}C_3N_4$ (Fig. 12b). To analyze the above performance enhancement mechanism, the EPR spectra were carried out and presented in Fig. 12c. In contrast to the pure $g\text{-}C_3N_4$, the Cu_3P and $Cu_3P/g\text{-}C_3N_4$ samples exhibited much stronger DMPO-·O_2^- signals, revealing that photoinduced electrons on Cu_3P possessed enough reducing capacity to involve in reduction reaction and did not migrate to the CB of $g\text{-}C_3N_4$. In other words, the carrier transmission way between Cu_3P and $g\text{-}C_3N_4$ followed the S-scheme heterojunction mechanism (Fig. 12d), contributing to their significantly improved CO_2 reduction performance.

In addition, the most recently reported $g\text{-}C_3N_4$-based S-scheme heterojunctions for CO_2 reduction have been displayed in Table 2 [32,37,86–100]. Generally, $g\text{-}C_3N_4$ could be fabricated S-scheme heterojunctions with many other semiconductors due to its excellent band structure. For instance, Bashal *et al.* [89] synthesized a Cu nanoparticle-modified $g\text{-}C_3N_4/MoS_2$ S-scheme heterojunction photocatalyst. The as-prepared $Cu/g\text{-}C_3N_4/MoS_2$ composite presented an extremely strong CO_2 reduction rate of ca. 146.7 μmol h^{-1} g^{-1}, over 9-fold higher than that of $g\text{-}C_3N_4$. Tahir *et al.* [94] developed a Ti_3AlC_2 MAX cocatalyst-modified $g\text{-}C_3N_4/TiO_2$ heterojunction photocatalyst *via* a sol-gel dip-coating strategy. The resultant Ti_3AlC_2 MAX-$g\text{-}C_3N_4/TiO_2$ composite exhibited a significantly reinforced CO_2 reduction activity of ca. 2400.7 μmol h^{-1} g^{-1}, which is over 23 times superior to the pure $g\text{-}C_3N_4$. The above evidently reinforced CO_2 reduction performance could be mainly due to the fact that the charge transfer route of the generated $g\text{-}C_3N_4/TiO_2$ heterojunction obeyed the S-scheme mechanism.

Pollutant degradation

With the advancement of global industrialization, environmental pollution has become increasingly serious, and the content of various pollutants, such as oxynitrides, antibiotics, and dyes, in the atmosphere, water, and soil has seriously exceeded the standard [101]. Therefore, it is urgent to seek effective methods to remove these environmental pollutants. Among the many processing strategies, photocatalytic degradation technique can effectively remove the pollutants in the atmosphere, water, and soil, and the degradation process of pollutants is mild and does not produce toxic substances. Moreover, the effect of the photocatalyst cycle is not reduced, and it can be recycled and reused. Based on the photocatalytic degradation mechanism, the more positive the VB of the semiconductor, the more stronger oxidation capacity of its photogenerated holes, thus efficiently degrading various pollutants into non-toxic and harmless CO_2 and H_2O. However, $g\text{-}C_3N_4$, a typical RP, usually presents very weak photocatalytic degradation activity due to its limited oxidation capacity and severe recombination of carriers. In this case, combining the OPs with $g\text{-}C_3N_4$ to form S-scheme heterojunctions could effectively solve the problem of weak oxidation capacity and severe recombination of carriers for $g\text{-}C_3N_4$, thus greatly enhancing its photocatalytic degradation activity.

For instance, Van Pham *et al.* [102] constructed a $g\text{-}C_3N_4/$

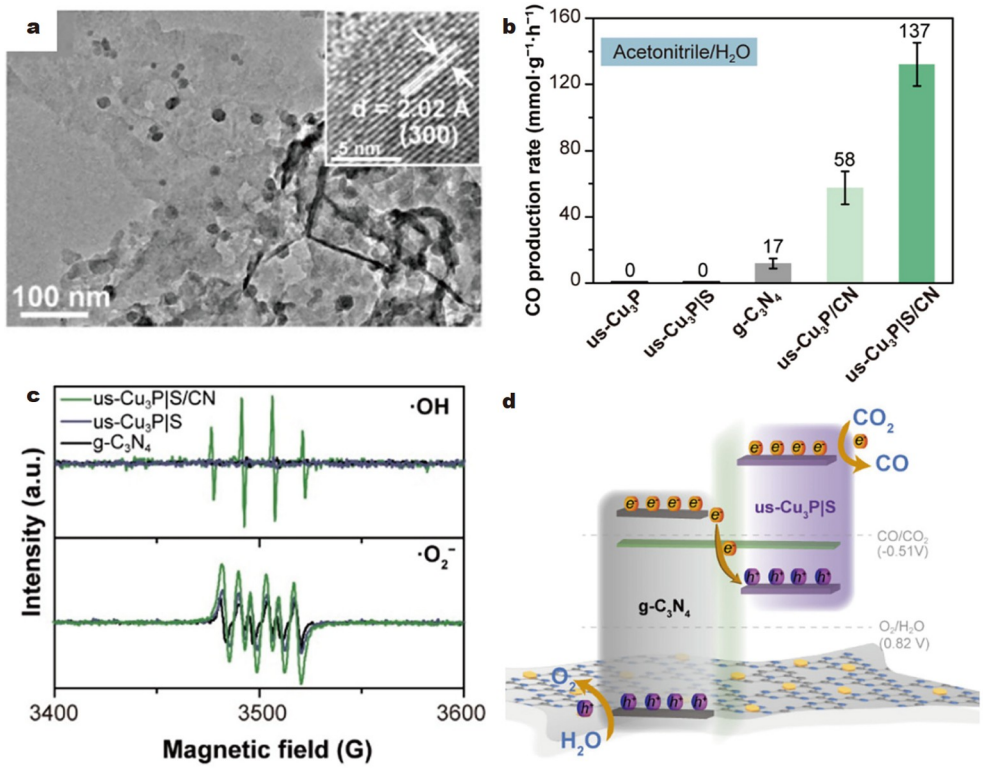

Figure 12 (a) TEM and HRTEM (inset) images of us-Cu_3P/S/CN. (b) CO_2 reduction activity. (c) EPR spectra and (d) S-scheme mechanism. Reprinted with permission from Ref. [88]. Copyright 2021, American Chemical Society.

Table 2 Recently reported g-C_3N_4-based S-scheme heterojunctions for CO_2 reduction

S-scheme heterojunction	Light source (wavelength/nm)	Reduction products	CO_2 reduction rate (μmol h^{-1} g^{-1})	Enhancement factor *versus* g-C_3N_4	Apparent quantum yield (%)	Ref.
$InVO_4$ QDs/g-C_3N_4	300 W Xe lamp (λ > 420 nm)	CO (93.3%)	69.8	18	6.8	[32]
O-g-C_3N_4/N-Nb_2O_5	300 W Xe lamp	CO (78.82%) CH_4 (21.18%)	321.5	6	4.9	[37]
TiO_2/g-C_3N_4	300 W Xe lamp	CO CH_4	785.3	5.9	–	[86]
g-C_3N_4/Cu_2O@Cu	300 W Xe lamp	CO CH_4	13.9	–	–	[87]
Cu_3P/g-C_3N_4	300 W Xe lamp	CO	137	9	–	[88]
g-C_3N_4/MoS_2/Cu	350 W Xe lamp (λ > 420 nm)	CO (100%)	146.7	9.7	3.2	[89]
g-C_3N_4/BiOBr	300 W Xe	CH_3OH	267	–	–	[90]
g-C_3N_4/Pd/MoO_{3-x}	300 W Xe lamp	CO	4.6	12.1	0.01	[91]
Ti_3C_2-g-C_3N_4/$MoSe_2$	Simulated sunlight	CO CH_4	47.8	–	–	[92]
g-C_3N_4/Ag-TiO_2	300 W Xe lamp	CO CH_4	52.7	–	2.4	[93]
g-C_3N_4/TiO_2/Ti_3AlC_2 MAX	35 W HID car lamp	CO (3.41%) CH_4 (96.59%)	2400.8	23.3	–	[94]
$ZnIn_2S_4$/g-C_3N_4	300 W Xe lamp	CO	883	13.4	8.9	[95]
$CsPbBr_3$/S-g-C_3N_4	300 W Xe lamp (λ > 400 nm)	CO	83.6	4	–	[96]
Bi_3NbO_7/g-C_3N_4	Simulated solar	CH_4 (90%)	37.6	15	–	[97]
BiOI/g-C_3N_4	300 W Xe lamp (λ > 400 nm)	CO	3.1	5.4	–	[98]
g-C_3N_4/ZnO	300 W Xe lamp	CH_4	16	7	–	[99]
rGO/R-CeO_2/g-C_3N_4	300 W Xe lamp	CO CH_4	23.9	4.6	–	[100]

SnO_2 S-scheme heterojunction *via* a facile calcination process, involving the pre-synthesizing SnO_2 nanoparticles and g-C_3N_4 nanosheets by simple hydrothermal and calcination treatments, respectively (Fig. 13a). The HRTEM image of g-C_3N_4/SnO_2 composite clearly emerged that SnO_2 nanoparticles with different sizes were loaded on g-C_3N_4 nanosheet surface (Fig. 13b), investigating the successful production of g-C_3N_4/SnO_2 heterojunction. Additionally, the as-constructed g-C_3N_4/SnO_2 heterojunction showed obviously reinforced photocatalytic NO removal activity, which is 1.2 times higher than that of pure g-C_3N_4 (Fig. 13c). The above enhanced photocatalytic activity could be primarily owing to the fact that the generated g-C_3N_4/SnO_2 S-scheme heterojunction could effectively promote carrier transmission and enhance its oxidation capacity (Fig. 13d).

Generally, semiconductors with strong oxidation ability are mostly metal oxides. Hence, g-C_3N_4 is usually combined with various metal oxides to construct S-scheme heterojunctions and applied in photocatalytic degradation. For another example, Truong and co-workers [103] fabricated a novel α-Fe_2O_3/g-C_3N_4 S-scheme heterojunction by a simple sonication treatment, including the pre-synthesizing α-Fe_2O_3 and g-C_3N_4 *via* sol-gel method and calcination process (Fig. 14a). The as-fabricated α-Fe_2O_3/g-C_3N_4 heterojunction displayed prominently reinforced photocatalytic degradation performance of cefalexin and amoxicillin, which was 5-fold and 9-fold superior to the pure g-C_3N_4, respectively (Fig. 14b, c). To reveal the above performance enhancement mechanism, EPR spectra were conducted. Obviously, under visible light, the DMPO-·O_2^- and DMPO-·OH signals could be clearly detected in g-C_3N_4 and α-Fe_2O_3/g-C_3N_4 samples, while they could not be detected in dark (Fig. 14d, e). Combining the active-radical trapping test results, it was not difficult to draw a conclusion that the carrier transmission way obeyed the S-scheme heterojunction (Fig. 14f), which contributed to the significantly enhanced degradation rate of α-Fe_2O_3/g-C_3N_4.

Except for metal oxides, some oxysalt semiconductors are also often used to construct S-scheme heterojunctions with g-C_3N_4. For instance, Dai *et al.* [104] produced an Au/g-C_3N_4/$BiO_{1.2}I_{0.6}$ photocatalyst (Fig. 15a) by a facile calcination method. The TEM and HRTEM images of the resultant Au/g-C_3N_4/$BiO_{1.2}I_{0.6}$ sample clearly showed the lattice fringes of characteristic crystal faces for Au and $BiO_{1.2}I_{0.6}$ (Fig. 15b, c). Moreover, the semitransparent and amorphous lamellar structures of g-C_3N_4 could be observed, powerfully indicating the successful production of Au/g-C_3N_4/$BiO_{1.2}I_{0.6}$ heterojunction structure. Additionally, the as-designed Au/g-C_3N_4/$BiO_{1.2}I_{0.6}$ sample displayed excellent photoreduction activity of Cr(VI) and photocatalytic degradation activity of BPAF, which were 3.7 and 6.5 times higher than that of the pure

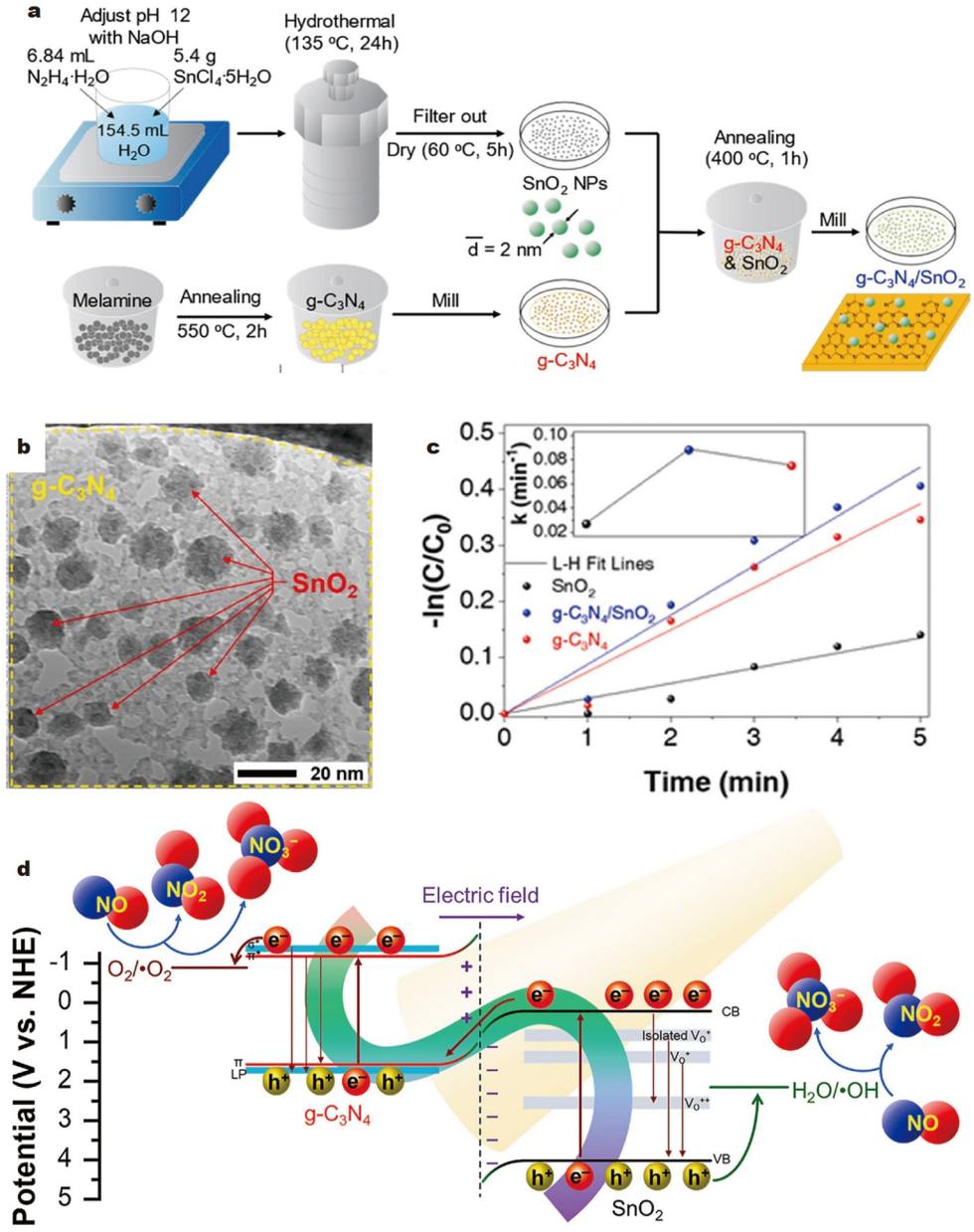

Figure 13 (a) Synthetic process and (b) HRTEM image of g-C_3N_4/SnO_2 somposite. (c) NO degradation rate constants and (d) photocatalytic reaction mechanism. Reprinted with permission from Ref. [102]. Copyright 2021, Elsevier.

g-C_3N_4 (Fig. 15d, e), respectively. The characterization and theoretical calculation results indicated that the plasmon resonance effect of Au and the formation of S-scheme heterojunction jointly promoted the enhancement of photocatalytic performance for Au/g-C_3N_4/$BiO_{1.2}I_{0.6}$ sample.

In addition to the above examples, the most recently reported g-C_3N_4-based S-scheme heterojunctions for photocatalytic degradation contaminant are shown in Table 3 [68,102–163]. It is found that photocatalytic degradation technology can be applied to degrade various antibiotics, dyes, atmospheric pollutants, and even remove toxic heavy metal ions. Moreover, most of the reported g-C_3N_4-based S-scheme heterojunctions show extremely increased photocatalytic degradation activity. For instance, Mkhalid *et al.* [105] prepared a g-C_3N_4/Li_2MnO_3 heterojunction photocatalyst by a simple evaporation process. The obtained g-C_3N_4/Li_2MnO_3 heterojunction exhibited an obviously reinforced photocatalytic degradation rate of trichloroethylene, which was over 5-fold superior to the pure g-C_3N_4. Moreover, the improvement was mainly owing to the generation of S-scheme heterojunction, which significantly promoted the separation and transmission of photoinduced charges. Van et al. [106] constructed a g-C_3N_4/CdS nano-heterojunction *via* a solvothermal method. The as-prepared g-C_3N_4/CdS heterojunction emerged with an extremely increased photocatalytic degradation rate of methylene blue, nearly 25 times higher than that of pure g-C_3N_4, primarily due to the construction of S-scheme heterojunction between g-C_3N_4 and CdS.

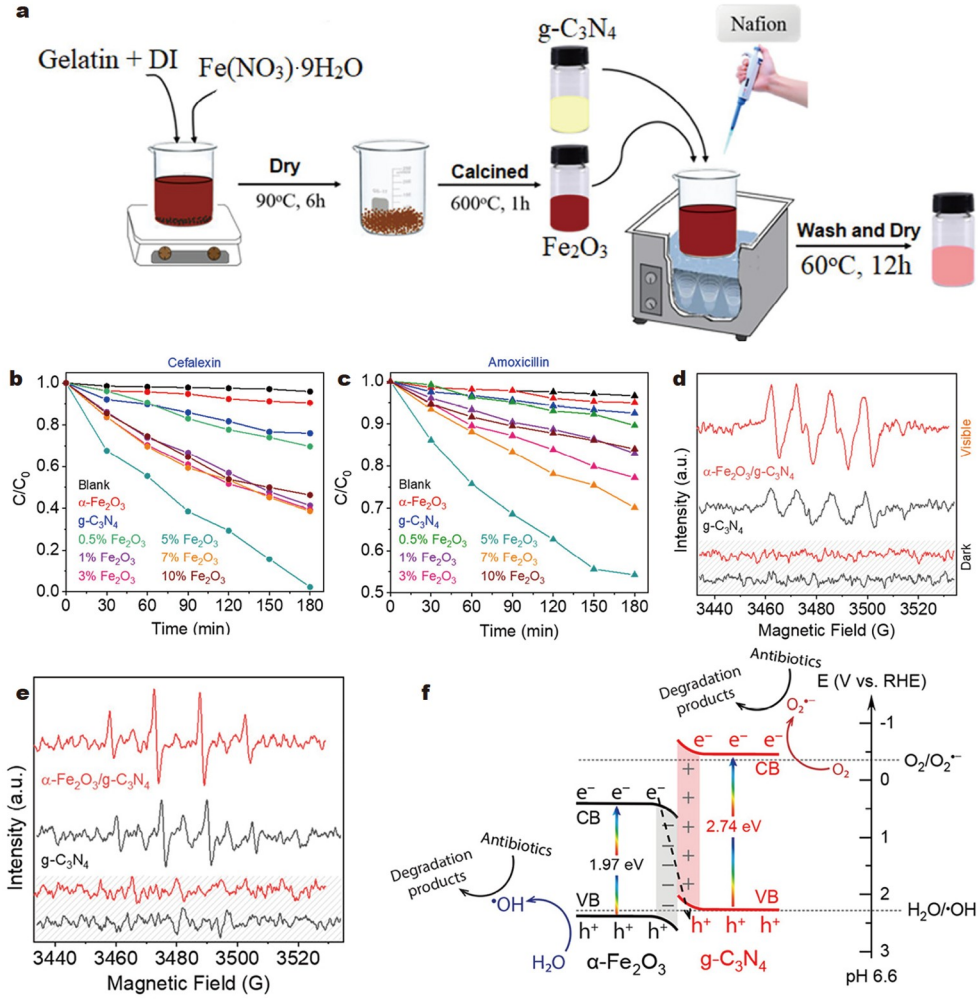

Figure 14 (a) Synthetic process of α-Fe_2O_3/g-C_3N_4. Photocatalytic degradation of (b) cefalexin and (c) amoxicillin. EPR signals of (d) DMPO-·O_2^- and (e) DMPO-·OH. (f) Photocatalytic mechanism. Reprinted with permission from Ref. [103]. Copyright 2022, American Chemical Society.

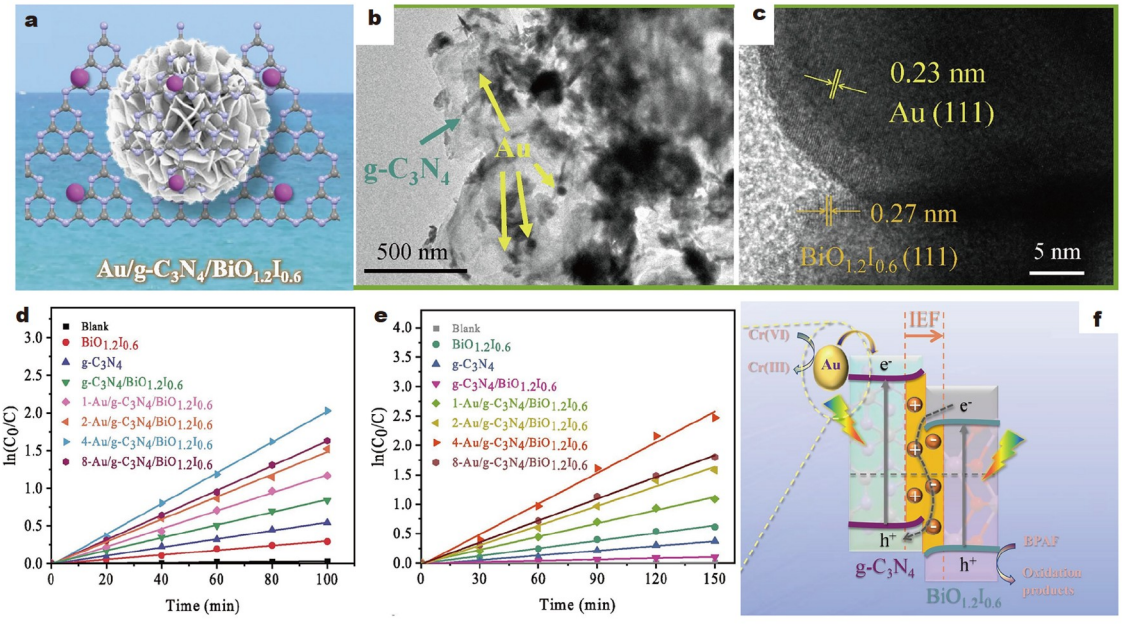

Figure 15 (a) Graphical illustration. (b) TEM and (c) HRTEM images of Au/g-C_3N_4/$BiO_{1.2}I_{0.6}$. Kinetic fitting photodegradation curves of (d) Cr(VI) and (e) BPAF. (f) Photocatalytic mechanism. Reprinted with permission from Ref. [104]. Copyright 2022, Elsevier.

Table 3 Recently reported g-C_3N_4-based S-scheme heterojunctions for pollutant degradation

S-scheme heterojunction	Light source (wavelength/nm)	Degradation substrate	Reduction rate (min^{-1})	Enhancement factor *versus* g-C_3N_4	Ref.
$Ti_{0.7}Sn_{0.3}O_2$/g-C_3N_4	1.5 W LED lamp	Rhodamine B	0.205	2.2	[68]
		Tetracycline hydrochloride	0.053	8.8	
g-C_3N_4/SnO_2	300 W Xe lamp ($400 < \lambda < 800$ nm)	NO	0.0881	1.2	[102]
α-Fe_2O_3/g-C_3N_4	300W Osram lamp ($\lambda > 420$ nm)	Cefalexin	0.0113	5.0	[103]
		Amoxicillin	0.004	9.0	
Au/g-C_3N_4/$BiO_{1.2}I_{0.6}$	500 W Xe lamp ($\lambda > 420$ nm)	Bisphenol AF	0.0174	6.5	[104]
		Cr (VI)	0.0204	3.7	
Li_2MnO_3/g-C_3N_4	300 W Xe lamp ($\lambda > 420$ nm)	Trichloroethylene	0.0127	6.7	[105]
CdS/g-C_3N_4	30 W LED lamp	Methylene blue	0.025	25	[106]
Bi_2MoO_6(2 0 0)/g-C_3N_4	Xe lamp ($\lambda > 420$ nm)	Hg^0	–	–	[107]
R.palustris/RCM@CPU	500 W Xe lamp ($\lambda > 420$ nm)	Azo dye	–	–	[108]
g-C_3N_4/TiO_2	300 W Xe lamp	Methylene Blue	0.0548	5.4	[109]
		Tetracycline	0.3154	8.5	
TiO_2/g-C_3N_4	350 W Xe lamp	LBW	0.0023	2.9	[110]
g-C_3N_4/$Mn(VO_3)_2$	500 W Xe lamp	Sulfamethoxazole	–	14	[111]
$LaFeO_3$/g-C_3N_4	1000 W Xe lamp	RB-19	0.0239	24.8	[112]
		Cr (VI)	0.0172	10.3	
$ZnFe_2O_4$/g-C_3N_4	300 W Xe lamp	Tetracycline hydrochloride	0.0454	4.6	[113]
g-C_3N_4/BiOI	Xe lamp ($\lambda > 420$ nm)	Tetracycline	0.1687	27.2	[114]
		Cr (VI)	0.0718	8.5	
g-C_3N_4/$NiFe_2O_4$	300 W Xe lamp	Tetracycline	0.0145	2.3	[115]
CeO_2-C-g-C_3N_4	250 W Xe lamp ($320 < \lambda < 780$ nm)	Methylene blue	0.0567	2.4	[116]
		Tetracyclines	0.0194	1.5	
TiO_{2-x}/g-C_3N_4/CNFe	300 W Xe lamp ($\lambda > 420$ nm)	Peroxymonosulfate	0.0969	–	[117]
g-C_3N_4/WO_3/ZnS	300 W Xe lamp ($\lambda > 420$ nm)	Tetracycline	0.042	3.5	[118]
O-g-C_3N_4/OV BiOCl	500 W Xe lamp ($\lambda > 400$ nm)	Bisphenol A	0.035	12.1	[119]
MgO/g-C_3N_4	300 W Xe lamp ($\lambda > 420$ nm)	Rhodamine B	0.0064	33.7	[120]
g-C_3N_4/GO/$ZnFe_2O_4$	Halogen lamp	Tetracycline	–	–	[121]
		Rhodamine B	–	–	
		Methylene Blue	–	–	
g-C_3N_4/CeO_2	300 W Xe lamp	Bisphenol A	0.0257	8.6	[122]
g-C_3N_4/TiO_2/$ZnIn_2S_4$/GA	300 W Xe lamp	Methyl orange	0.094	37.6	[123]
		Cr (VI)	0.0411	9.3	
$La_2Ce_2O_7$/g-C_3N_4	300 W Xe lamp ($\lambda > 420$ nm)	Rhodamine B	0.027	2.4	[124]
g-C_3N_4/$TiOF_2$	500 W Xe lamp	Tetracycline hydrochloride	1.052	2.8	[125]
N-TiO_{2-x}/g-C_3N_4	300 W Xe lamp ($\lambda > 400$ nm)	2,4-dinitrophenylhydrazine	–	–	[126]
α-Fe_2O_3/g-C_3N_4	300 W Xe lamp	Tetracycline hydrochloride	0.0165	3.1	[127]
Ag_2CO_3/$Bi_4O_5I_2$/g-C_3N_4	300 W Xe lamp	Tetracycline	0.0389	13.3	[128]
N-g-C_3N_4/NH_2-MIL-125(Ti)	300 W Xe lamp ($\lambda > 400$ nm)	Rhodamine B	0.0246	3.3	[129]
$CaSnO_3$/g-C_3N_4	500 W Halogen lamp	Methylene Blue	–	–	[130]

(*To be continued on the next page*)

(*Continued*)

S-scheme heterojunction	Light source (wavelength/nm)	Degradation substrate	Reduction rate (min^{-1})	Enhancement factor *versus* g-C_3N_4	Ref.
SnO_{2-x}/g-C_3N_4	300 W Osram lamp (λ > 420 nm)	NO	–	–	[131]
g-C_3N_4/Ag/AgNCO	300 W Xe lamp	Tetracycline	0.3	3.1	[132]
g-C_3N_4/SnO_2	300 W Xe lamp	NO	–	–	[133]
α-Fe_2O_3/g-C_3N_4	300 W Xe lamp (λ > 420 nm)	Tetracycline	–	–	[134]
N-ZnO/g-C_3N_4	300 W Xe lamp	Norfloxacin	0.034	4.1	[135]
SnO_2/g-C_3N_4	30 W LED lamp	Rhodamine B	0.0353	10.7	[136]
PDI/g-C_3N_4/TiO_2@Ti_3C_2	300 W Xe lamp (λ > 420 nm)	Atrazine	0.0248	4.4	[137]
WO_3/g-C_3N_4	300 W Solar simulation light	NO	0.119	2.1	[138]
g-C_3N_4/$BiVO_4$	300 W Xe lamp (λ > 400 nm)	Methylene blue	0.0609	15.2	[139]
MoO_3/g-C_3N_4	300 W Xe lamp	Rhodamine B Cr (VI)	– –	– –	[140]
g-C_3N_4/TiO_2/CFs	350 W Xe lamp	Tetracycline hydrochloride	0.1566	9.5	[141]
BiOBr/Ni_2P/g-C_3N_4	300 W Xe lamp ($\lambda \geq$ 400 nm)	Rhodamine B Methyl orange	0.026 0.0154	3.6 3.9	[142]
Bi_2Se_3/g-C_3N_4	60 W LED lamp (λ > 400 nm)	Phenol	–	–	[143]
g-C_3N_4/TiO_2	UV light	Tetracycline hydrochloride	0.057	–	[144]
TiO_2/CN QDs	500 W Xe lamp	Methyl orange	0.0172	–	[145]
g-C_3N_4/Mo-WO_3	350 W Xe lamp	Methyl orange	0.0367	14.1	[146]
g-C_3N_4/$ZnIn_2S_4$	LED lamp (λ > 400 nm)	Tetracycline	0.0196	2.5	[147]
g-C_3N_4/NiZnAl-LDH	500 W Xe lamp (λ < 400 nm)	Methyl orange Tetracycline	0.0233 0.0145	3.5 3.2	[148]
g-C_3N_4/rGO/ZnO-Ag	–	Rhodamine B Methyl orange	0.017 0.023	5.7 4.9	[149]
BiOBr/g-C_3N_4	500 W Xe lamp (λ > 400 nm)	Ethyl xanthate	0.0282	24.6	[150]
SnS_2/g-C_3N_4	60 W lamp (200 < λ < 400 nm)	Rhodamine B	0.0074	4.2	[151]
$CoTiO_3$/g-C_3N_4	300 W Xe lamp (λ > 400 nm)	Methyl orange	0.0165	38.1	[152]
g-C_3N_4/MXene/Ag_3PO_4	300 W Xe lamp ($\lambda \geq$ 420 nm)	Tetracycline	0.0353	4.3	[153]
$ZnFe_2O_4$/g-C_3N_4	300 W Xe lamp ($\lambda \geq$ 400 nm)	Bisphenol A	0.075	–	[154]
$Bi_4V_2O_{11}$/g-C_3N_4	300 W Xe lamp (λ > 420 nm)	Oxytetracycline	–	3.3	[155]
BiOBr/g-C_3N_4	300 W Xe lamp (λ > 400 nm)	Rhodamine B	0.0127	48.2	[156]
$ZnFe_2O_4$/g-C_3N_4	LED lamp	Uranium (VI)	–	–	[157]
Bi_2WO_6/g-C_3N_4	300 W Xe lamp (λ > 400 nm)	Ammonium dinitramide	0.0567	44.3	[158]
S-g-C_3N_4/TiO_2	300 W Xe lamp	Congo Red	0.0962	8.2	[159]
$Cd_{0.5}Zn_{0.5}S$/g-C_3N_4	350 W Xe lamp (λ > 420 nm)	Rhodamine B	0.0817	13	[160]
C-WO_3/g-C_3N_4	300 W Xe lamp (λ > 420 nm)	Tetracycline	0.0378	2.3	[161]
Bi_2MoO_6/g-C_3N_4	300 W Xe lamp (λ > 420 nm)	Rhodamine B	0.0808	9.7	[162]
g-C_3N_4/α-Fe_2O_3	Halogen lamp	Methyl orange	0.029	–	[163]

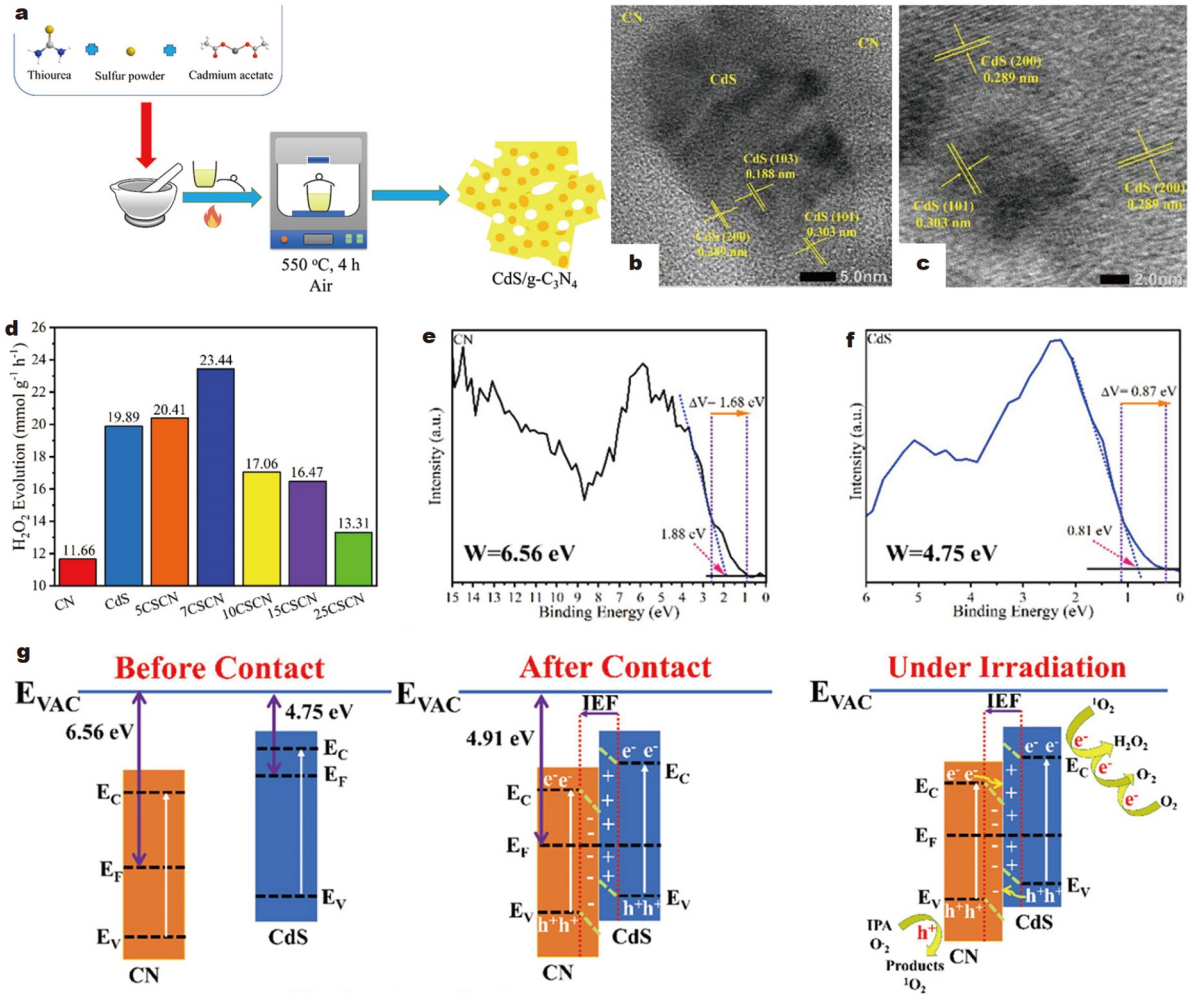

Figure 16 (a) Preparation process. (b, c) HRTEM images. (d) H_2O_2 production rates. Work functions of (e) g-C_3N_4 and (f) CdS. (g) S-scheme mechanism. Reprinted with permission from Ref. [165]. Copyright 2023, American Chemical Society.

H_2O_2 production

Hydrogen peroxide (H_2O_2), a powerful oxidizing agent and bleach, has been broadly used in industry, aerospace, energy, and other fields due to its advantages of pollution-free, green, and clean [164]. Currently, the anthraquinone method is mainly used to produce H_2O_2. However, the anthraquinone method always causes high energy consumption, large carbon, organic solvents and pollutants emission. Therefore, developing environmentally friendly, efficient, and economical strategy to produce H_2O_2 is just what the public wanted. Based on the fact, photocatalytic H_2O_2 production can convert H_2O and O_2 into H_2O_2 driven by sunlight. Namely, H_2O_2 can be efficiently produced by a suitable photocatalyst [85]. According to the mechanism of photocatalytic production H_2O_2, currently reported H_2O_2 generation is mainly based on photogenerated electron reduction reaction. In this case, g-C_3N_4 has been broadly used to produce H_2O_2.

For example, Phan *et al.* [165] designed a g-C_3N_4/CdS S-scheme heterojunction *via* a plain calcination strategy (Fig. 16a). The HRTEM images of g-C_3N_4/CdS composite indicated that CdS particles were aggregated on the surface of amorphous g-C_3N_4. Moreover, the lattice fringes corresponding to (103), (101), and (200) crystal faces could be clearly observed (Fig. 16b, c). Additionally, the resultant g-C_3N_4/CdS heterojunction emerged with a prominent H_2O_2 production rate of 23,440 μmol h^{-1} g^{-1}, which was over two times superior to the pure g-C_3N_4 (Fig. 16d), primarily owing to the generated g-C_3N_4/CdS S-scheme heterojunction. To demonstrate the formation process of S-scheme heterojunction, the work functions of g-C_3N_4 and CdS were calculated and shown in Fig. 16e, f. Due to their different work functions, the free electrons of CdS would migrate to the g-C_3N_4 when they came into contact, thus generating a built-in electric field direction from CdS to g-C_3N_4 (Fig. 16g). When they were excited by the light, the photogenerated carrier with weak redox ability would recombine, while the carrier with strong redox ability would be retained and participated in the following interface reaction, thus contributing to their highly increased performance.

Except for metal sulfides, g-C_3N_4 is also often coupled with some metal oxides to construct S-scheme heterojunction and used to produce H_2O_2. For instance, Wang and co-workers [166] designed a Pd-modified Cu_2O/g-C_3N_4 S-scheme heterojunction photocatalyst. The TEM image revealed that the Cu_2O-Pd particles were glomerated onto the surface of the semitransparent g-C_3N_4 framework (Fig. 17a). Moreover, the lattice fringes and spacings corresponding to Cu_2O and Pd could be clearly observed from their HRTEM images in Fig. 17b, c. Simulta-

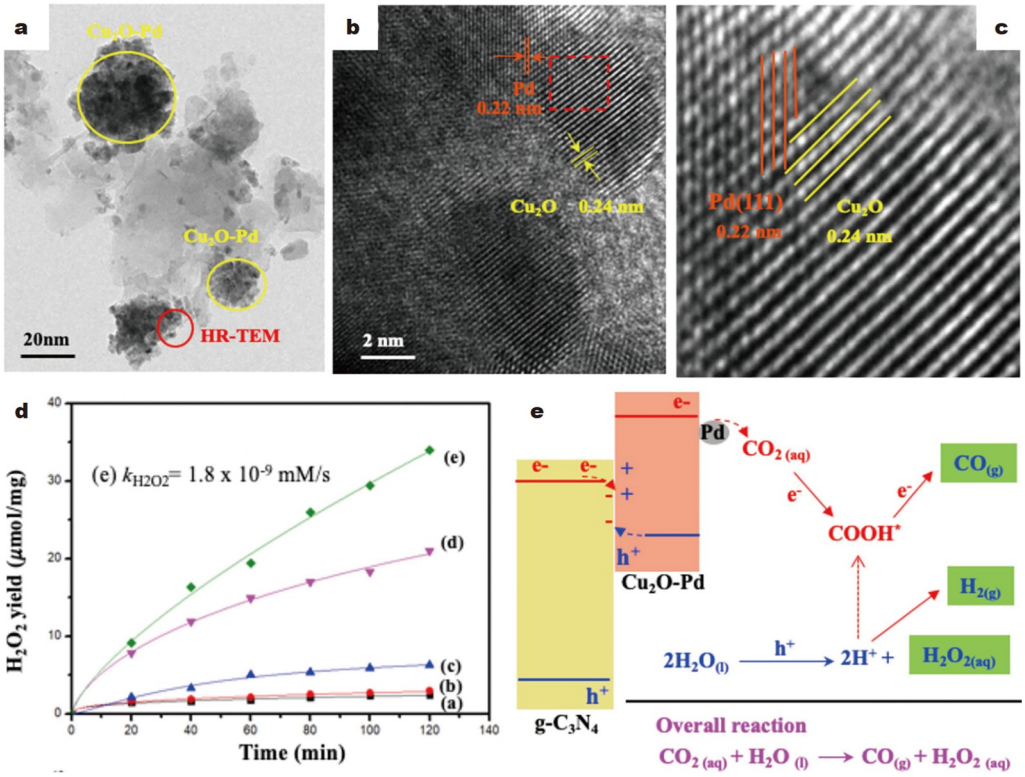

Figure 17 (a) TEM and (b, c) HRTEM images of g-C_3N_4/Cu_2O-Pd sample. (d) H_2O_2 production rates and (e) H_2O_2 production and charge transfer mechanism. Reprinted with permission from Ref. [166]. Copyright 2023, American Chemical Society.

neously, the lattice fringes of Cu_2O and Pd emerged obvious intersections (Fig. 17c), adequately indicating the successful generation of Pd-modified Cu_2O/g-C_3N_4 heterojunction structures. Additionally, the resultant g-C_3N_4/Cu_2O-Pd sample exhibited a super-strong H_2O_2 production rate of 34,000 μmol h^{-1} g^{-1}, which was over 10-fold stronger than that of pure g-C_3N_4 (Fig. 17d). The greatly improved performance can be mainly ascribed to the synergistic promotion of S-scheme heterojunction and Pd modification (Fig. 17e).

In addition to the above metal oxides and sulfides, metal-organic frameworks have been broadly combined with g-C_3N_4 to produce heterojunction photocatalysts. For example, Xia *et al.* [167] fabricated a novel g-C_3N_4/Zinc porphyrin (Zn-TCPP) S-scheme heterojunction photocatalyst by a thermal polycondensation route. The as-prepared g-C_3N_4/Zn-TCPP heterojunction composite presented an evidently improved H_2O_2 production-rate of 355.13 μmol h^{-1} g^{-1}, over 3-fold superior to the g-C_3N_4 (Fig. 18a). Moreover, the g-C_3N_4/Zn-TCPP could maintain its initial high performance after four H_2O_2-production cycles (Fig. 18b). To demonstrate the charge transfer route between g-C_3N_4 and Zn-TCPP, KPFM technology was conducted, and its corresponding results were provided in Fig. 18c–f. In dark, the surface potential of Zn-TCPP (point B, 402 mV) was obviously higher than that of g-C_3N_4 (point A, 101 mV), which would cause the migration of electrons from Zn-TCPP to g-C_3N_4, thus producing a built-in electric field of direction from Zn-TCPP to g-C_3N_4 (Fig. 18g). With light illumination, the surface potential of g-C_3N_4 (point A) increased even more, due to the fact that the photoinduced electrons migrated from g-C_3N_4 to Zn-TCPP, consistent with the direction of the electric field. Consequently, the above KPFM results *in-situ* confirmed the carrier transmission path of S-scheme heterojunction.

In addition to the above examples, the most recently reported g-C_3N_4-based S-scheme heterojunctions for H_2O_2 production are displayed in Table 4 [165–174]. It is found that g-C_3N_4 can be used to construct S-scheme heterojunctions with various oxidation and reduction-type photocatalysts and show significantly enhanced activity. For instance, Fang *et al.* [168] designed a hollow sphere structure Pt/g-C_3N_4/BiOBr S-scheme heterojunction *via* a solvothermal method. The resultant Pt/g-C_3N_4/BiOBr heterojunction exhibited a prominent H_2O_2-production rate of 225 μmol h^{-1} g^{-1}. Das *et al.* [169] developed a Fe_2O_3 quantum dots/boron-doped g-C_3N_4 (Fe_2O_3 QD/B-g-C_3N_4) S-scheme heterojunction photocatalyst by an *in-situ* generation strategy. The resultant Fe_2O_3 QD/B-g-C_3N_4 heterojunction showed an obviously reinforced H_2O_2-production rate of 729 μmol h^{-1} g^{-1}, nearly two times higher than the pure g-C_3N_4, mainly due to the generation of S-scheme heterojunction between Fe_2O_3 QD and B-g-C_3N_4. Consequently, all the reported g-C_3N_4-based S-scheme heterojunctions displayed excellent photocatalytic H_2O_2 production performance.

Other applications

Except for the above applications of photocatalytic degradation, H_2 evolution, H_2O_2 production, and CO_2 reduction, g-C_3N_4-based S-scheme heterojunction photocatalysts have also been used to produce O_2 and fixate nitrogen (N_2). For instance, Li *et al.* [175] constructed a g-C_3N_4/Ag_3PO_4 S-scheme heterojunction through an in-situ synthetic strategy, involving the premier fabrication of g-C_3N_4 nanotube and the next *in-situ* production of Ag_3PO_4 onto g-C_3N_4 (Fig. 19a). The obtained g-

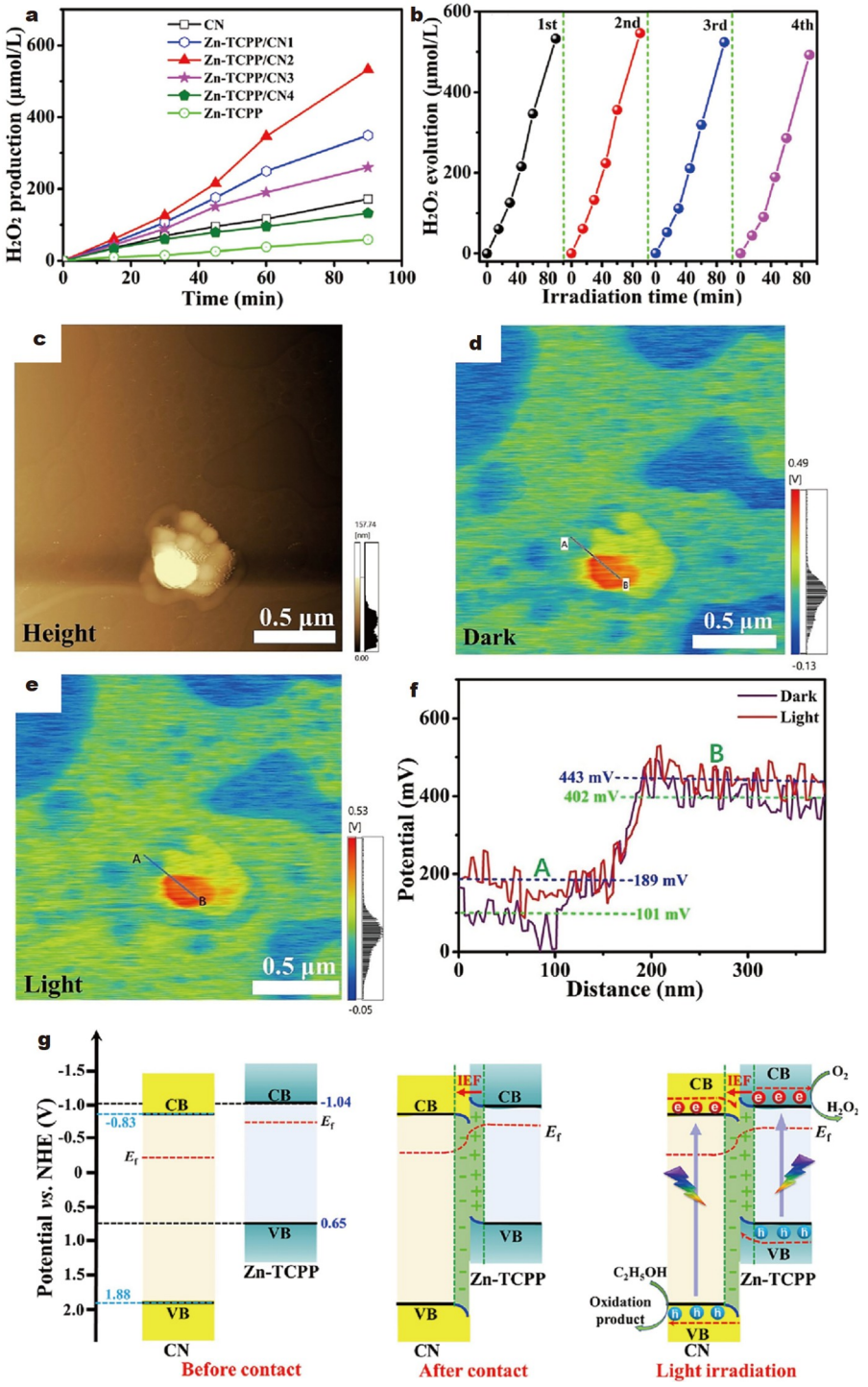

Figure 18 (a) H_2O_2 production rates. (b) Recycling tests. (c) AFM image and the corresponding surface potential maps: (d) dark and (e) light. (f) Surface potentials from A to B and (g) S-scheme mechanism. Reprinted with permission from Ref. [167]. Copyright 2023, Elsevier.

C_3N_4/Ag_3PO_4 heterojunction composite displayed an excellent photocatalytic O_2-production rate of ca. 370.2 μmol L^{-1} h^{-1}, over 3-fold superior to the pure Ag_3PO_4 (Fig. 19b). The above enhancements could be mainly due to the fact that the generated g-C_3N_4/Ag_3PO_4 S-scheme heterojunction significantly improved the migration efficiency and redox ability of carriers.

N_2 fixation technology is essential for the development of industry and agriculture. The proportion of N_2 in the air is as high as 78%. However, most plant corpus cannot directly absorb and utilize the N_2 in the air. Traditional industrial ammonia synthesis can convert N_2 into ammonia that is easily absorbed by organisms, while it requires high temperature, high pressure, and H_2 energy as a raw material. Therefore, there is an urgent need to develop new, gentle, and green technologies to convert abundant nitrogen into nitrogen that can be absorbed by living organisms. Photocatalytic N_2-fixation technology is driven by solar energy, N_2, and water as raw materials; N_2 can be converted into ammonia easily absorbed by organisms. For instance,

Table 4 Recently reported g-C_3N_4-based S-scheme heterojunction photocatalysts for H_2O_2 evolution

S-scheme heterojunction	Sacrificial agent	Light source (wavelength/nm)	H_2O_2 production rate (μmol h^{-1} g^{-1})	Enhancement factor *versus* g-C_3N_4	Apparent quantum yield (%)	Ref.
CdS/g-C_3N_4	–	3 × 50 W Halogen lamp	23,440	2	–	[165]
g-C_3N_4/Cu_2O-Pd	–	500 W Xe lamp ($\lambda > 400$ nm)	34,000	–	3.3	[166]
Zn-TCPP/g-C_3N_4	Ethanol	300 W Xe lamp	355.1	3.1	7	[167]
Pt/g-C_3N_4/BiOBr	–	300 W Xe lamp ($\lambda > 400$ nm)	225	–	–	[168]
Fe_2O_3 QD/B-g-C_3N_4	5% IPA	250 W Hg lamp ($\lambda \geq 420$ nm)	729	2	–	[169]
S-g-C_3N_4/TiO_2	–	300 W Xe lamp ($300 \leq \lambda \leq 700$ nm)	2128	2.6	0.6	[170]
PCN/MnS	–	300 W Xe lamp	4188	–	8.5	[171]
CN QDs/BiOBr	–	300 W Xe lamp	–	–	–	[172]
NH_2-MIL-101(Fe) @MCN/Bi_2O_3	–	300 W Xe lamp ($\lambda > 420$ nm)	327.8	2.7	–	[173]
g-C_3N_4/PDA	–	300 W Xe lamp ($\lambda > 350$ nm)	3801.3	2	2.2	[174]

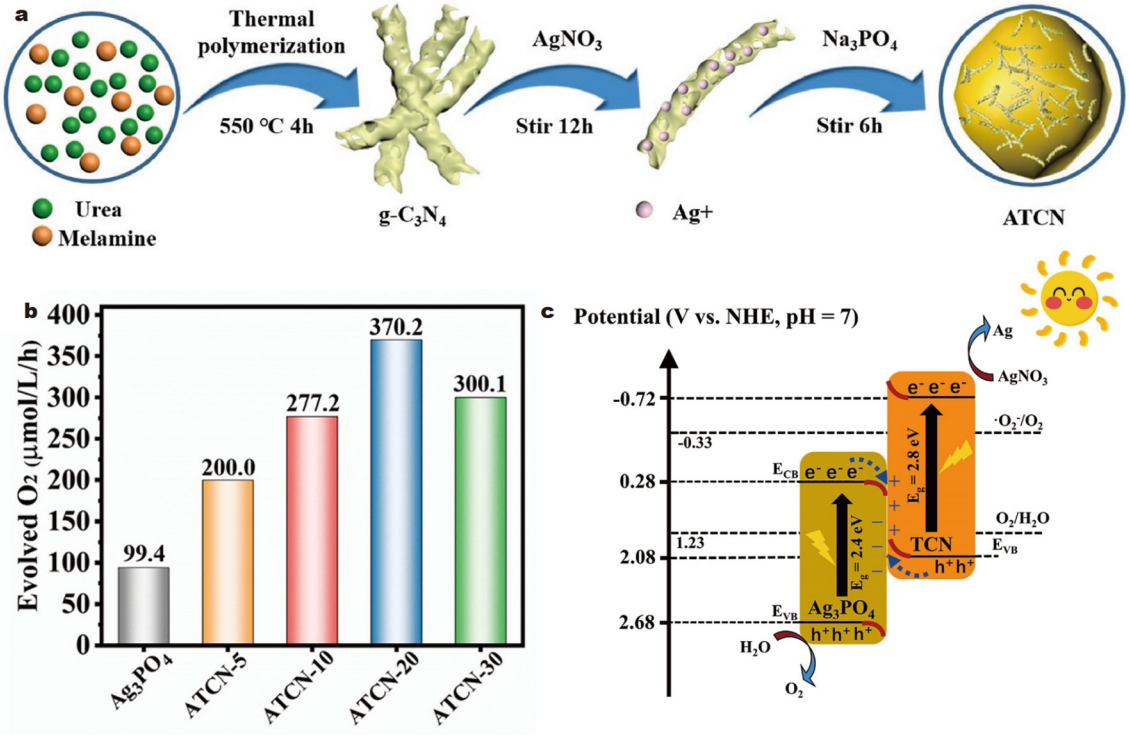

Figure 19 (a) Synthesis process. (b) O_2 production rates and (c) photocatalytic mechanism. Reprinted with permission from Ref. [175]. Copyright 2022, Elsevier.

Mousavi *et al.* [176] constructed a g-C_3N_4/$AgBiS_2$ S-scheme heterojunction photocatalyst *via* a solvothermal method. The TEM image (Fig. 20a) shows that $AgBiS_2$ aggregates were attached to the surface of translucent g-C_3N_4 nanosheets (CNNS). Moreover, the lattice fringes and spacings corresponding to CNNS(002) and $AgBiS_2$(200) could be clearly observed from its HRTEM image in Fig. 20b. Additionally, the resultant g-C_3N_4/$AgBiS_2$ heterojunction exhibited prominent N_2-fixation (NH_4^+ generation) activity of ca. 3780 μmol g^{-1} L^{-1}, over 2-fold and 3-fold higher than that of pure $AgBiS_2$ and g-C_3N_4, respectively (Fig. 20c). Moreover, the g-C_3N_4/$AgBiS_2$ sample emerged excellent stability in the cycle test of nitrogen-fixation performance (Fig. 20d). The above excellent N_2-fixation activity and stability were mainly due to the fact that the S-scheme g-C_3N_4/$AgBiS_2$ heterojunction could efficiently accelerate charge transmission efficiency and enhance its redox ability.

CONCLUSIONS AND OUTLOOK

In summary, single-component photocatalysts cannot simultaneously possess high utilization efficiency of solar energy and strong redox abilities of photoexcited charges, thus usually suffering weak photocatalytic activity [177,178]. The star material g-C_3N_4 in the field of photocatalysis is no exception. In this case,

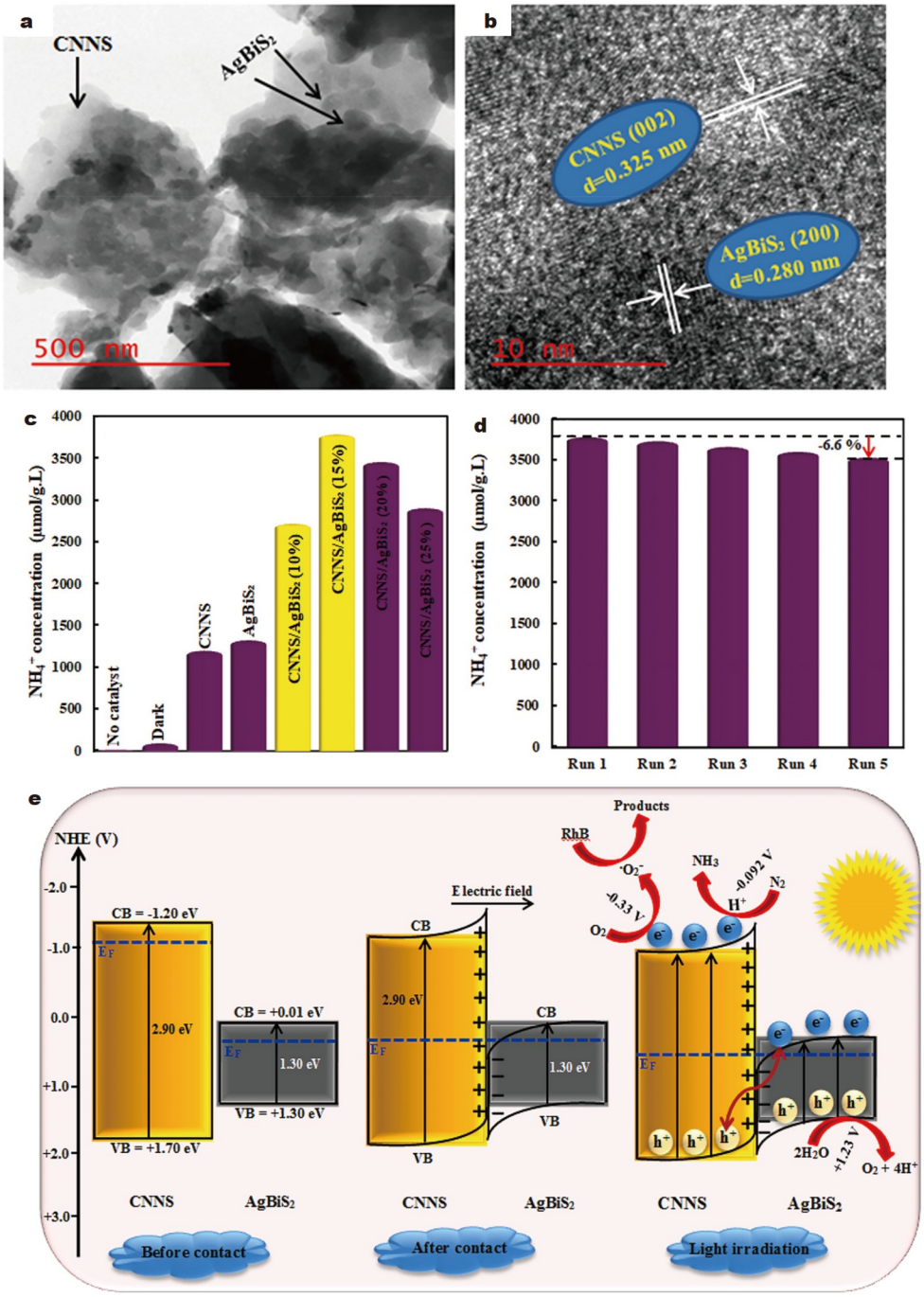

Figure 20 (a) TEM and (b) HRTEM images of CNNS/$AgBiS_2$. (c) Photocatalytic N_2 fixation activities. (d) Recycling tests and (e) photocatalytic mechanism. Reprinted with permission from Ref. [176]. Copyright 2023, Elsevier.

constructing S-scheme heterojunctions between g-C_3N_4 with other semiconductors can simultaneously overcome the typical shortcomings of low light energy utilization, rapid recombination, and weak redox abilities of carriers, thus prominently reinforcing its photocatalytic performance [179]. Hence, this review comprehensively comments on the latest research progress of background, fundamental theory, design and preparation, and characterization strategies of g-C_3N_4-based S-scheme heterojunctions. Additionally, various photocatalytic applications of g-C_3N_4-based S-scheme heterojunctions have been detailly illustrated through example discussion and list comparison, involving photocatalytic H_2 production, CO_2 reduction, H_2O_2 production, pollutant degradation, and others.

Although g-C_3N_4-based S-scheme heterojunctions have made phased progress in controllable construction and enhancement of activity, there are still some bottlenecks to overcome, which are listed as follows.

(1) The dynamic process of charge transfer and the intensity, position, and direction of the built-in electric field are still lacking *in-situ* characterization methods to intuitively reveal. It is well-known that revealing the S-scheme mechanism in depth is the prerequisite for its further development. Therefore, there is

an urgent need to develop new characterization technologies to effectively reveal the mechanism. Meanwhile, it is necessary to strengthen interdisciplinary integration to intuitively and efficiently detect the relevant information of the built-in electric field.

(2) According to the carrier transmission path of S-scheme heterojunction, it is not difficult to conclude that the interfacial electric field is the key factor driving the transmission of photoexcitation charges in S-scheme heterojunctions. However, the current researches for the improvement of g-C_3N_4-based S-scheme heterojunction are primarily concentrating on the traditional cocataltyst modification, element doping, morphology regulation, etc. [180–183], and the influences of the built-in electric field of S-scheme heterojunction on its carrier separation efficiency and photocatalytic activity are rarely studied. Therefore, it is extremely indispensable to investigate the regulation of interfacial built-in electric field of g-C_3N_4-based S-scheme heterojunction and its relationship with photocatalytic activity.

(3) As we all know, there is a certain gap between the current photocatalysis efficiency and the industrial application level, which is the key bottleneck of current photocatalysis technology. Improving the efficiency of photocatalysis technology to a level that can be used industrially is the ultimate goal. Therefore, future research should optimize every condition that can improve the activity of the photocatalytic systems from the inside out. Taking the study of g-C_3N_4-based S-scheme heterojunction as an example, the intrinsic structure (such as morphology, specific surface area, and crystallinity) of g-C_3N_4 and other semiconductors, the heterojunction interface structure, the related interfacial electric field structure, and other factors need to be optimized to break through the bottleneck of performance improvement and reach the level of industrial application.

Received 30 November 2023; accepted 4 January 2024; published online 24 January 2024

1 Xiang X, Wang L, Zhang J, *et al.* Cadmium chalcogenide (CdS, CdSe, CdTe) quantum dots for solar-to-fuel conversion. Adv Photonics Res, 2022, 3: 2200065
2 Sayed M, Yu J, Liu G, *et al.* Non-noble plasmonic metal-based photocatalysts. Chem Rev, 2022, 122: 10484–10537
3 Gao D, Long H, Wang X, *et al.* Tailoring antibonding-orbital occupancy state of selenium in Se-enriched $ReSe_{2+x}$ cocatalyst for exceptional H_2 evolution of TiO_2 photocatalyst. Adv Funct Mater, 2023, 33: 2209994
4 Yang Y, Wu J, Cheng B, *et al.* Enhanced photocatalytic H_2 production activity of CdS nanoflower using single atom Pt and graphene quantum dot as dual cocatalysts. Chin J Struct Chem, 2022, 41: 2206006–2206014
5 Bie C, Cheng B, Ho W, *et al.* Graphdiyne-based photocatalysts for solar fuel production. Green Chem, 2022, 24: 5739–5754
6 Wang M, Wang P, Wang X, *et al.* Self-optimized H-adsorption affinity of CuRu alloy cocatalysts towards efficient photocatalytic H_2 evolution. J Mater Sci Tech, 2024, 174: 168–175
7 Xu J, Zhong W, Zhang X, *et al.* Triggering the channel-sulfur sites in 1T′-ReS_2 cocatalyst toward splendid photocatalytic hydrogen generation. Small, 2023, 19: 2303960
8 Yang Y, Cheng B, Yu J, *et al.* TiO_2/In_2S_3 S-scheme photocatalyst with enhanced H_2O_2-production activity. Nano Res, 2021, 16: 4506–4514
9 Bie C, Zhu B, Wang L, *et al.* A bifunctional CdS/MoO_2/MoS_2 catalyst enhances photocatalytic H_2 evolution and pyruvic acid synthesis. Angew Chem Int Ed, 2022, 61: e202212045
10 Zhao B, Zhong W, Chen F, *et al.* High-crystalline g-C_3N_4 photocatalysts: Synthesis, structure modulation, and H_2-evolution application. Chin J Catal, 2023, 52: 127–143
11 Wu X, Gao D, Yu H, *et al.* High-yield lactic acid-mediated route for a g-C_3N_4 nanosheet photocatalyst with enhanced H_2-evolution performance. Nanoscale, 2019, 11: 9608–9616
12 Bie C, Wang L, Yu J. Challenges for photocatalytic overall water splitting. Chem, 2022, 8: 1567–1574
13 Gao D, Deng P, Zhang J, *et al.* Reversing free-electron transfer of MoS_{2+x} cocatalyst for optimizing antibonding-orbital occupancy enables high photocatalytic H_2 evolution. Angew Chem Int Ed, 2023, 62: e202304559
14 Zhong W, Xu J, Zhang X, *et al.* Charging d-orbital electron of ReS_{2+x} cocatalyst enables splendid alkaline photocatalytic H_2 evolution. Adv Funct Mater, 2023, 33: 2302325
15 He B, Wang Z, Xiao P, *et al.* Cooperative coupling of H_2O_2 production and organic synthesis over a floatable polystyrene-sphere-supported TiO_2/Bi_2O_3 S-scheme photocatalyst. Adv Mater, 2022, 34: 2203225
16 Zhang L, Zhang J, Yu H, *et al.* Emerging S-scheme photocatalyst. Adv Mater, 2022, 34: 2107668
17 Cao S, Yu J, Wageh S, *et al.* H_2-production and electron-transfer mechanism of a noble-metal-free WO_3@$ZnIn_2S_4$ S-scheme heterojunction photocatalyst. J Mater Chem A, 2022, 10: 17174–17184
18 Serpone N, Borgarello E, Grätzel M. Visible light induced generation of hydrogen from H_2S in mixed semiconductor dispersions, improved efficiency through inter-particle electron transfer. J Chem Soc Chem Commun, 1984, 6: 342–344
19 Sayama K, Mukasa K, Abe R, *et al.* A new photocatalytic water splitting system under visible light irradiation mimicking a Z-scheme mechanism in photosynthesis. J Photochem Photobiol A-Chem, 2002, 148: 71–77
20 Tada H, Mitsui T, Kiyonaga T, *et al.* All-solid-state Z-scheme in CdS-Au-TiO_2 three-component nanojunction system. Nat Mater, 2006, 5: 782–786
21 Wang Z, Cheng B, Zhang L, *et al.* S-scheme 2D/2D Bi_2MoO_6/BiOI van der Waals heterojunction for CO_2 photoreduction. Chin J Catal, 2022, 43: 1657–1666
22 Fu J, Xu Q, Low J, *et al.* Ultrathin 2D/2D WO_3/g-C_3N_4 step-scheme H_2-production photocatalyst. Appl Catal B-Environ, 2019, 243: 556–565
23 Cheng C, Zhu B, Cheng B, *et al.* Catalytic conversion of styrene to benzaldehyde over S-scheme photocatalysts by singlet oxygen. ACS Catal, 2023, 13: 459–468
24 Han G, Xu F, Cheng B, *et al.* Enhanced photocatalytic H_2O_2 production over inverse opal ZnO@ polydopamine S-scheme heterojunctions. Acta Physico Chim Sin, 2022, 0: 2112037–0
25 Wageh S, Al-Ghamdi AA, Al-Hartomy OA, *et al.* CdS/polymer S-scheme H_2-production photocatalyst and its *in-situ* irradiated electron transfer mechanism. Chin J Catal, 2022, 43: 586–588
26 Wang L, Zhang J, Yu H, *et al.* Dynamics of photogenerated charge carriers in inorganic/organic S-scheme heterojunctions. J Phys Chem Lett, 2022, 13: 4695–4700
27 Zhang J, Wang L, Mousavi M, *et al.* Molecular-level engineering of S-scheme heterojunction: The site-specific role for directional charge transfer. Chin J Struct Chem, 2022, 41: 2206003–2206005
28 Xu Q, Wageh S, Al-Ghamdi AA, *et al.* Design principle of S-scheme heterojunction photocatalyst. J Mater Sci Tech, 2022, 124: 171–173
29 Wu X, Ma H, Zhong W, *et al.* Porous crystalline g-C_3N_4: Bifunctional $NaHCO_3$ template-mediated synthesis and improved photocatalytic H_2-evolution rate. Appl Catal B-Environ, 2020, 271: 118899
30 Li Y, Xia Z, Yang Q, *et al.* Review on g-C_3N_4-based S-scheme heterojunction photocatalysts. J Mater Sci Tech, 2022, 125: 128–144
31 Wu X, Chen G, Li L, *et al.* $ZnIn_2S_4$-based S-scheme heterojunction photocatalyst. J Mater Sci Tech, 2023, 167: 184–204
32 Gong S, Teng X, Niu Y, *et al.* Construction of S-scheme 0D/2D heterostructures for enhanced visible-light-driven CO_2 reduction. Appl Catal B-Environ, 2021, 298: 120521
33 Cheng C, Zhang J, Zhu B, *et al.* Verifying the charge-transfer mechanism in S-scheme heterojunctions using femtosecond transient absorption spectroscopy. Angew Chem Int Ed, 2023, 62: e202218688
34 Wu X, Chen G, Wang J, *et al.* Review on S-scheme heterojunctions for photocatalytic hydrogen evolution. Acta Physico Chim Sin, 2023, 0:

2212016
35 Wang L, Cheng B, Zhang L, *et al. In situ* irradiated XPS investigation on S-scheme TiO_2@$ZnIn_2S_4$ photocatalyst for efficient photocatalytic CO_2 reduction. Small, 2021, 17: 2103447
36 Zhang J, Zhang L, Wang W, *et al. In situ* irradiated X-ray photoelectron spectroscopy investigation on electron transfer mechanism in S-scheme photocatalyst. J Phys Chem Lett, 2022, 13: 8462–8469
37 Qaraah FA, Mahyoub SA, Hezam A, *et al.* Synergistic effect of hierarchical structure and S-scheme heterojunction over O-doped g-C_3N_4/N-doped Nb_2O_5 for highly efficient photocatalytic CO_2 reduction. Appl Catal B-Environ, 2022, 315: 121585
38 Cheng C, He B, Fan J, *et al.* An inorganic/organic S-scheme heterojunction H_2-production photocatalyst and its charge transfer mechanism. Adv Mater, 2021, 33: 2100317
39 Xu Q, Zhang L, Cheng B, *et al.* S-scheme heterojunction photocatalyst. Chem, 2020, 6: 1543–1559
40 Wu X, Ma H, Wang K, *et al.* High-yield and crystalline graphitic carbon nitride photocatalyst: One-step sodium acetate-mediated synthesis and improved hydrogen-evolution performance. J Colloid Interface Sci, 2023, 633: 817–827
41 Wu X, Gao D, Wang P, *et al.* NH_4Cl-induced low-temperature formation of nitrogen-rich g-C_3N_4 nanosheets with improved photocatalytic hydrogen evolution. Carbon, 2019, 153: 757–766
42 Li S, Wang Y, Wang J, *et al.* Efficient photocatalytic hydrogen evolution reaction promoted *via* a synergistic strategy of S-scheme heterojunction structure combined with surface plasmon resonance effect. Chem Eng J, 2023, 466: 143184
43 Shi WL, Xu Z, Shi YX, *et al.* Constructing S-scheme charge separation in cobalt phthalocyanine/oxygen-doped g-C_3N_4 heterojunction with enhanced photothermal-assisted photocatalytic H_2 evolution. Rare Met, 2024, 43: 198–211
44 Zhu B, Tan H, Fan J, *et al.* Tuning the strength of built-in electric field in 2D/2D g-C_3N_4/SnS_2 and g-C_3N_4/ZrS_2 S-scheme heterojunctions by nonmetal doping. J Materiomics, 2021, 7: 988–997
45 Hafeez HY, Mohammed J, Ndikilar CE, *et al.* Synergistic utilization of magnetic rGO/$NiFe_2O_4$-g-C_3N_4 S-scheme heterostructure photocatalyst with enhanced charge carrier separation and transfer: A highly stable and robust photocatalyst for efficient solar fuel (hydrogen) generation. Ceramics Int, 2023, 49: 5269–5278
46 Hassan AE, Elsayed MH, Hussien MSA, *et al.* V_2O_5 nanoribbons/N-deficient g-C_3N_4 heterostructure for enhanced visible-light photocatalytic performance. Int J Hydrogen Energy, 2023, 48: 9620–9635
47 Zhang J, Zhao Y, Qi K, *et al.* $CuInS_2$ quantum-dot-modified g-C_3N_4 S-scheme heterojunction photocatalyst for hydrogen production and tetracycline degradation. J Mater Sci Tech, 2024, 172: 145–155
48 Zhu Z, Zhang H, Teng Y, *et al.* Enhanced photocatalytic hydrogen evolution over Ce-TiO_2/graphite/g-C_3N_4 ternary S-scheme heterojunction. Surfs Interfaces, 2023, 41: 103160
49 Sun T, Li C, Bao Y, *et al.* S-scheme $MnCo_2S_4$/g-C_3N_4 heterojunction photocatalyst for H_2 production. Acta Physico Chim Sin, 2023, 0: 2212009
50 Mo X, Zhang X, Lin B, *et al.* Boosting interfacial S-scheme charge transfer and photocatalytic H_2-production activity of 1D/2D WO_3/g-C_3N_4 heterojunction by molecular benzene-rings integration. J Mater Sci Tech, 2023, 145: 174–184
51 Fang W, Yang Y, Liu J, *et al.* Self-assembly core-shell $Bi_xY_{1-x}VO_4$@g-C_3N_4 as an S-scheme heterojunction photocatalyst for pure water splitting. Int J Hydrogen Energy, 2023, 48: 25379–25389
52 Lei Z, Cao X, Fan J, *et al.* Efficient photocatalytic H_2 generation over $In_{2.77}S_4$/NiS_2/g-C_3N_4 S-scheme heterojunction using NiS_2 as electron-bridge. Chem Eng J, 2023, 457: 141249
53 Alam U, Pandey A, Verma N. An anthraquinone-integrated S-scheme-based $NiTiO_3$-g-C_3N_4 composite with enhanced hydrogen production activity. Int J Hydrogen Energy, 2023, 48: 2532–2541
54 Shang Y, Fan H, Yang X, *et al.* Synergism between chemisorption and unique electron transfer pathway in S-scheme AgI/g-C_3N_4 heterojunction for improving the photocatalytic H_2 evolution. J Colloid Interface Sci, 2023, 631: 269–280
55 Sun X, Li L, Hu T, *et al.* In_2S_3/g-C_3N_4/CoZnAl-LDH composites with the lamellar dual S-scheme heterostructure and its enhanced photocatalytic performance. Colloids Surfs A-Physicochem Eng Aspects, 2023, 658: 130744
56 Xu Z, Zhong J, Chen J, *et al.* Construction of S-scheme Co_3O_4/g-C_3N_4 heterojunctions with boosted photocatalytic H_2 production performance. Surfs Interfaces, 2023, 38: 102838
57 Wang D, Miao C, Zhao X, *et al.* Construction of Co-doped Sn_3O_4/g-C_3N_4 heterojunction with enhanced interface transmission capability for improving hydrogen production. Ceramics Int, 2023, 49: 27724–27732
58 Yang J, Wu X, Mei Z, *et al.* CVD assisted synthesis of macro/mesoporous TiO_2/g-C_3N_4 S-scheme heterojunction for enhanced photocatalytic hydrogen evolution. Adv Sustain Syst, 2022, 6: 2200056
59 Mu F, Dai B, Wu Y, *et al.* 2D/3D S-scheme heterojunction of carbon nitride/iodine-deficient bismuth oxyiodide for photocatalytic hydrogen production and bisphenol A degradation. J Colloid Interface Sci, 2022, 612: 722–736
60 Jiang J, Xiong Z, Wang H, *et al.* Sulfur-doped g-C_3N_4/g-C_3N_4 isotype step-scheme heterojunction for photocatalytic H_2 evolution. J Mater Sci Tech, 2022, 118: 15–24
61 Zhao Z, Dai K, Zhang J, *et al. In situ* preparation of $Mn_{0.2}Cd_{0.8}S$-diethylenetriamine/porous g-C_3N_4 S-scheme heterojunction with enhanced photocatalytic hydrogen production. Adv Sustain Syst, 2023, 7: 2100498
62 Shi W, Sun W, Liu Y, *et al.* Onion-ring-like g-C_3N_4 modified with Bi_3TaO_7 quantum dots: A novel 0D/3D S-scheme heterojunction for enhanced photocatalytic hydrogen production under visible light irradiation. Renew Energy, 2022, 182: 958–968
63 Feng K, Tian J, Hu X, *et al.* Active-center-enriched $Ni_{0.85}Se$/g-C_3N_4 S-scheme heterojunction for efficient photocatalytic H_2 generation. Int J Hydrogen Energy, 2022, 47: 4601–4613
64 Zhou H, Ke J, Wu H, *et al.* Manganese tungstate/graphitic carbon nitride S-scheme heterojunction for boosting hydrogen evolution and mechanism exploration. Mater Today Energy, 2022, 23: 100918
65 Zhang Q, Bai X, Hu X, *et al.* Efficient photocatalytic H_2 evolution over 2D/2D S-scheme $NiTe_2$/g-C_3N_4 heterojunction with superhydrophilic surface. Appl Surf Sci, 2022, 579: 152224
66 Bi F, Su Y, Zhang Y, *et al.* Vacancy-defect semiconductor quantum dots induced an S-scheme charge transfer pathway in 0D/2D structures under visible-light irradiation. Appl Catal B-Environ, 2022, 306: 121109
67 Li X, Zhang J, Huo Y, *et al.* Two-dimensional sulfur- and chlorine-codoped g-C_3N_4/CdSe-amine heterostructures nanocomposite with effective interfacial charge transfer and mechanism insight. Appl Catal B-Environ, 2021, 280: 119452
68 Guo B, Liu B, Wang C, *et al.* S-scheme $Ti_{0.7}Sn_{0.3}O_2$/g-C_3N_4 heterojunction composite for enhanced photocatalytic pollutants degradation. J Environ Chem Eng, 2022, 10: 107118
69 Dai B, Li Y, Xu J, *et al.* Photocatalytic oxidation of tetracycline, reduction of hexavalent chromium and hydrogen evolution by Cu_2O/g-C_3N_4 S-scheme photocatalyst: Performance and mechanism insight. Appl Surf Sci, 2022, 592: 153309
70 Ran Y, Cui Y, Zhang Y, *et al.* Assembly-synthesis of puff pastry-like g-C_3N_4/CdS heterostructure as S-junctions for efficient photocatalytic water splitting. Chem Eng J, 2022, 431: 133348
71 Li C, Zhao Y, Fan J, *et al.* Nanoarchitectonics of S-scheme 0D/2D $SbVO_4$/g-C_3N_4 photocatalyst for enhanced pollution degradation and H_2 generation. J Alloys Compd, 2022, 919: 165752
72 Wang D, Lin Z, Miao C, *et al.* An S-scheme photocatalyst constructed by modifying Ni-doped Sn_3O_4 micro-flowers on g-C_3N_4 nanosheets for enhanced visible-light-driven hydrogen evolution. J Industrial Eng Chem, 2022, 113: 380–388
73 Chen Y, Wang Q, Huang H, *et al.* Effective solar driven H_2 production by $Mn_{0.5}Cd_{0.5}Se$/g-C_3N_4 S-scheme heterojunction photocatalysts. Int J Hydrogen Energy, 2021, 46: 32514–32522
74 Chen X, Ke X, Zhang J, *et al.* Insight into the synergy of amine-modified S-scheme $Cd_{0.5}Zn_{0.5}Se$/porous g-C_3N_4 and noble-metal-free Ni_2P for boosting photocatalytic hydrogen generation. Ceramics Int, 2021, 47: 13488–13499

75 Chen Y, Su F, Xie H, *et al.* One-step construction of S-scheme heterojunctions of N-doped MoS_2 and S-doped g-C_3N_4 for enhanced photocatalytic hydrogen evolution. Chem Eng J, 2021, 404: 126498
76 Li X, Kang B, Dong F, *et al.* Enhanced photocatalytic degradation and H_2/H_2O_2 production performance of S-pCN/$WO_{2.72}$ S-scheme heterojunction with appropriate surface oxygen vacancies. Nano Energy, 2021, 81: 105671
77 Ren D, Zhang W, Ding Y, *et al. In situ* fabrication of robust cocatalyst-free CdS/g-C_3N_4 2D-2D step-scheme heterojunctions for highly active H_2 evolution. Sol RRL, 2020, 4: 1900423
78 Liu J, Wei X, Sun W, *et al.* Fabrication of S-scheme CdS-g-C_3N_4-graphene aerogel heterojunction for enhanced visible light driven photocatalysis. Environ Res, 2021, 197: 111136
79 Chen X, Hu T, Zhang J, *et al.* Diethylenetriamine synergistic boosting photocatalytic performance with porous g-C_3N_4/CdS-diethylenetriamine 2D/2D S-scheme heterojunction. J Alloys Compd, 2021, 863: 158068
80 Xu Q, Ma D, Yang S, *et al.* Novel g-C_3N_4/g-C_3N_4 S-scheme isotype heterojunction for improved photocatalytic hydrogen generation. Appl Surf Sci, 2019, 495: 143555
81 Shang Y, Wang C, Yan C, *et al.* An efficient and multifunctional S-scheme heterojunction photocatalyst constructed by tungsten oxide and graphitic carbon nitride: Design and mechanism study. J Colloid Interface Sci, 2023, 634: 195–208
82 Li H, Tao S, Wan S, *et al.* S-scheme heterojunction of ZnCdS nanospheres and dibenzothiophene modified graphite carbon nitride for enhanced H_2 production. Chin J Catal, 2023, 46: 167–176
83 Ding Q, Zou X, Ke J, *et al.* S-scheme 3D/2D $NiCo_2O_4$@g-C_3N_4 hybridized system for boosting hydrogen production from water splitting. Renew Energy, 2023, 203: 677–685
84 Wang Y, Xing Z, Yang Y, *et al.* Oxygen-Defective Bi_2MoO_6/g-C_3N_4 hollow tubulars S-scheme heterojunctions toward optimized photocatalytic performance. J Colloid Interface Sci, 2024, 653: 1566–1576
85 Wang L, Zhu B, Zhang J, *et al.* S-scheme heterojunction photocatalysts for CO_2 reduction. Matter, 2022, 5: 4187–4211
86 Wang L, Fei X, Zhang L, *et al.* Solar fuel generation over nature-inspired recyclable TiO_2/g-C_3N_4 S-scheme hierarchical thin-film photocatalyst. J Mater Sci Tech, 2022, 112: 1–10
87 Dai B, Zhao W, Wei W, *et al.* Photocatalytic reduction of CO_2 and degradation of Bisphenol-S by g-C_3N_4/Cu_2O@Cu S-scheme heterojunction: Study on the photocatalytic performance and mechanism insight. Carbon, 2022, 193: 272–284
88 Zhang X, Kim D, Yan J, *et al.* Photocatalytic CO_2 reduction enabled by interfacial S-scheme heterojunction between ultrasmall copper phosphosulfide and g-C_3N_4. ACS Appl Mater Interfaces, 2021, 13: 9762–9770
89 Bashal AH, Alkanad K, Al-Ghorbani M, *et al.* Synergistic effect of cocatalyst and S-scheme heterojunction over 2D/2D g-C_3N_4/MoS_2 heterostructure coupled Cu nanoparticles for selective photocatalytic CO_2 reduction to CO under visible light irradiation. J Environ Chem Eng, 2023, 11: 109545
90 Zhang T, Maihemllti M, Okitsu K, *et al. In situ* self-assembled S-scheme BiOBr/pCN hybrid with enhanced photocatalytic activity for organic pollutant degradation and CO_2 reduction. Appl Surf Sci, 2021, 556: 149828
91 Wang H, Liu Q, Xu M, *et al.* Dual-plasma enhanced 2D/2D/2D g-C_3N_4/Pd/MoO_{3-x} S-scheme heterojunction for high-selectivity photocatalytic CO_2 reduction. Appl Surf Sci, 2023, 640: 158420
92 Chen X, Pan W, Hong L, *et al.* Ti_3C_2-modified g-C_3N_4/$MoSe_2$ S-scheme heterojunction with full-spectrum response for CO_2 photoreduction to CO and CH_4. ChemSusChem, 2023, 16: e202300179
93 Zhang H, Bian H, Wang F, *et al.* Enhanced photocatalytic reduction of CO_2 over pg-C_3N_4-supported TiO_2 nanoparticles with Ag modification. Colloids Surfs A-Physicochem Eng Aspects, 2023, 674: 131989
94 Tahir M, Tahir B. Constructing S-scheme 2D/0D g-C_3N_4/TiO_2 NPs/MPs heterojunction with 2D-Ti_3AlC_2 MAX cocatalyst for photocatalytic CO_2 reduction to CO/CH_4 in fixed-bed and monolith photoreactors. J Mater Sci Tech, 2022, 106: 195–210
95 Li L, Ma D, Xu Q, *et al.* Constructing hierarchical $ZnIn_2S_4$/g-C_3N_4 S-scheme heterojunction for boosted CO_2 photoreduction performance. Chem Eng J, 2022, 437: 135153
96 Zhao T, Li D, Zhang Y, *et al.* Constructing built-in electric field within $CsPbBr_3$/sulfur doped graphitic carbon nitride ultra-thin nanosheet step-scheme heterojunction for carbon dioxide photoreduction. J Colloid Interface Sci, 2022, 628: 966–974
97 Wang K, Feng X, Shangguan Y, *et al.* Selective CO_2 photoreduction to CH_4 mediated by dimension-matched 2D/2D Bi_3NbO_7/g-C_3N_4 S-scheme heterojunction. Chin J Catal, 2022, 43: 246–254
98 Li H, Wang D, Miao C, *et al.* g-C_3N_4/BiOI S-scheme heterojunction: A 2D/2D model platform for visible-light-driven photocatalytic CO_2 reduction and pollutant degradation. J Environ Chem Eng, 2022, 10: 108201
99 Sayed M, Zhu B, Kuang P, *et al.* EPR investigation on electron transfer of 2D/3D g-C_3N_4/ZnO S-scheme heterojunction for enhanced CO_2 photoreduction. Adv Sustain Syst, 2022, 6: 2100264
100 Li X, Guan J, Jiang H, *et al.* rGO modified R-CeO_2/g-C_3N_4 multi-interface contact S-scheme photocatalyst for efficient CO_2 photoreduction. Appl Surf Sci, 2021, 563: 150042
101 Wageh S, Al-Ghamdi AA, Jafer R, *et al.* A new heterojunction in photocatalysis: S-scheme heterojunction. Chin J Catal, 2021, 42: 667–669
102 Van Pham V, Mai DQ, Bui DP, *et al.* Emerging 2D/0D g-C_3N_4/SnO_2 S-scheme photocatalyst: New generation architectural structure of heterojunctions toward visible-light-driven NO degradation. Environ Pollution, 2021, 286: 117510
103 Pham VV, Truong TK, Hai LV, *et al.* S-scheme α-Fe_2O_3/g-C_3N_4 nanocomposites as heterojunction photocatalysts for antibiotic degradation. ACS Appl Nano Mater, 2022, 5: 4506–4514
104 Dai B, Chen X, Yang X, *et al.* Designing S-scheme Au/g-C_3N_4/$BiO_{1.2}I_{0.6}$ plasmonic heterojunction for efficient visible-light photocatalysis. Sep Purif Technol, 2022, 287: 120531
105 Mkhalid IA, Mohamed RM, Alhaddad M, *et al.* S-scheme mesoporous Li_2MnO_3/g-C_3N_4 heterojunctions as efficient photocatalysts for the mineralization of trichloroethylene in aqueous media. J Colloid Interface Sci, 2022, 614: 160–171
106 Van KN, Huu HT, Nguyen Thi VN, *et al.* Construction of S-scheme CdS/g-C_3N_4 nanocomposite with improved visible-light photocatalytic degradation of methylene blue. Environ Res, 2022, 206: 112556
107 Zhang Y, Zhang S, Guo X, *et al.* Efficient Hg^0 catalytic removal by direct S-scheme heterostructure of two-dimensional Bi_2MoO_6 (2 0 0)/g-C_3N_4 nanosheets under visible light. J Environ Manage, 2023, 347: 119125
108 Liu K, Chen J, Sun F, *et al.* Enhanced degradation of azo dyes wastewater by S-scheme heterojunctions photocatalyst g-C_3N_4/MoS_2 intimately coupled Rhodopseudomonas palustris with chitosan modified polyurethane sponge carrier. Int J Hydrogen Energy, 2023, 48: 22319–22333
109 Wang J, Ren P, Du Y, *et al.* Construction of tubular g-C_3N_4/TiO_2 S-scheme photocatalyst for high-efficiency degradation of organic pollutants under visible light. J Alloys Compd, 2023, 947: 169659
110 Yang C, Zhang X, Zhou Y, *et al.* Well-designed MOF-derived hollow octahedral structure TiO_2 coupled with ultra-thin porous g-C_3N_4 to enhance the degradation of real liquor brewing wastewater. Appl Surf Sci, 2023, 616: 156471
111 Xu L, Dai R, Yang J, *et al.* A novel S-scheme g-C_3N_4/$Mn(VO_3)_2$ heterojunction photocatalyst for its superior photocatalytic degradation of broad-spectrum antibiotics. J Alloys Compd, 2023, 936: 168163
112 Hu C, Yu B, Zhu Z, *et al.* Construction of novel S-scheme $LaFeO_3$/g-C_3N_4 composite with efficient photocatalytic capacity for dye degradation and Cr(VI) reduction. Colloids Surfs A-Physicochem Eng Aspects, 2023, 664: 131189
113 Yan J, Chai B, Liu Y, *et al.* Construction of 3D/2D $ZnFe_2O_4$/g-C_3N_4 S-scheme heterojunction for efficient photo-Fenton degradation of tetracycline hydrochloride. Appl Surf Sci, 2023, 607: 155088
114 Dou K, Peng C, Wang R, *et al.* S-scheme tubular g-C_3N_4/BiOI heterojunctions for boosting photodegradation of tetracycline and Cr(VI): Mechanism insight, degradation pathway and DFT calculation. Chem Eng J, 2023, 455: 140813

115 Lu C, Wang J, Cao D, *et al.* Synthesis of magnetically recyclable g-C_3N_4/$NiFe_2O_4$ S-scheme heterojunction photocatalyst with promoted visible-light-response photo-Fenton degradation of tetracycline. Mater Res Bull, 2023, 158: 112064

116 Chu Z, Li J, Sohn HY, *et al.* CeO_2-g-C_3N_4 S-scheme heterojunctions for enhanced photocatalytic performance: Effects of surface C/N ratio on photocatalytic and adsorption properties. Compos Part B-Eng, 2023, 257: 110689

117 Li Z, Ai W, Zhang Y, *et al.* Magnetic carbon nanotube modified S-scheme TiO_{2-x}/g-C_3N_4/CNFe heterojunction coupled with peroxymonosulfate for effective visible-light-driven photodegradation *via* enhanced interfacial charge separation. Sep Purif Technol, 2023, 308: 122897

118 Sun H, Qin P, Guo J, *et al.* Enhanced electron channel *via* the interfacial heterotropic electric field in dual S-scheme g-C_3N_4/WO_3/ZnS photocatalyst for year-round antibiotic degradation under sunlight. Chem Eng J, 2023, 470: 144217

119 Zhang JJ, Di J, Zhao YP, *et al.* Synergistic defect and doping engineering building strong bonded S-scheme heterojunction for photocatalysis. Chemosphere, 2023, 344: 140347

120 Gao M, Li Z, Su X, *et al.* 2D/2D MgO/g-C_3N_4 S-scheme heterogeneous tight with Mg–N bonds for efficient photo-Fenton degradation: Enhancing both oxygen vacancy and charge migration. Chemosphere, 2023, 343: 140285

121 Kumar R, Sudhaik A, Raizada P, *et al.* Integrating K and P co-doped g-C_3N_4 with $ZnFe_2O_4$ and graphene oxide for S-scheme-based enhanced adsorption coupled photocatalytic real wastewater treatment. Chemosphere, 2023, 337: 139267

122 Xu Y, Tang X, Xiao Y, *et al.* Persulfate promoted visible photocatalytic elimination of bisphenol A by g-C_3N_4-CeO_2 S-scheme heterojunction: The dominant role of photo-induced holes. Chemosphere, 2023, 331: 138765

123 Liu H, Sun F, Li X, *et al.* g-C_3N_4/TiO_2/$ZnIn_2S_4$ graphene aerogel photocatalysts with double S-scheme heterostructure for improving photocatalytic multifunctional performances. Compos Part B-Eng, 2023, 259: 110746

124 Chen X, Li Z, Zhou J, *et al.* Constructing 2D/2D $La_2Ce_2O_7$/g-C_3N_4 S-scheme heterojunction for markedly enhanced interfacial charge separation and photocatalytic activity under visible light irradiation. J Alloys Compd, 2023, 960: 170892

125 Hou C, Niu M, Hao J, *et al.* Construction of an S-scheme g-C_3N_4/$TiOF_2$ heterostructures with abundant O vacancies: Enhanced photocatalytic activity and mechanism insight. J Alloys Compd, 2023, 938: 168560

126 Dong S, Chen S, He F, *et al.* Construction of a novel N-doped oxygen vacancy-rich TiO_2 N-TiO_{2-x}/g-C_3N_4 S-scheme heterostructure for visible light driven photocatalytic degradation of 2,4-dinitrophenylhydrazine. J Alloys Compd, 2022, 908: 164586

127 Xu F, Chai B, Liu Y, *et al.* Superior photo-Fenton activity toward tetracycline degradation by 2D α-Fe_2O_3 anchored on 2D g-C_3N_4: S-scheme heterojunction mechanism and accelerated Fe^{3+}/Fe^{2+} cycle. Colloids Surfs A-Physicochem Eng Aspects, 2022, 652: 129854

128 Chen ZJ, Guo H, Liu HY, *et al.* Construction of dual S-scheme Ag_2CO_3/$Bi_4O_5I_2$/g-C_3N_4 heterostructure photocatalyst with enhanced visible-light photocatalytic degradation for tetracycline. Chem Eng J, 2022, 438: 135471

129 Wang J, Chen C, Zhao Z, *et al.* Construction of N-doped g-C_3N_4/NH_2-MIL-125(Ti) S-scheme heterojunction for enhanced photocatalytic degradation of organic pollutants: DFT calculation and mechanism study. J Alloys Compd, 2022, 922: 166288

130 Venkatesh G, Palanisamy G, Srinivasan M, *et al.* $CaSnO_3$ coupled g-C_3N_4 S-scheme heterostructure photocatalyst for efficient pollutant degradation. Diamond Relat Mater, 2022, 124: 108873

131 Van Viet P, Nguyen TD, Bui DP, *et al.* Combining SnO_{2-x} and g-C_3N_4 nanosheets toward S-scheme heterojunction for high selectivity into green products of NO degradation reaction under visible light. J Materiomics, 2022, 8: 1–8

132 Fang H, Han Y, Feng X, *et al.* S-scheme heterojunction g-C_3N_4/Ag/AgNCO for efficient tetracycline removal in a photo-assisted peroxymonosulfate system. Sep Purif Technol, 2022, 296: 121210

133 Van Viet P, Nguyen HP, Tran HH, *et al.* Constructing g-C_3N_4/SnO_2 S-scheme heterojunctions for efficient photocatalytic NO removal and low NO_2 generation. J Sci-Adv Mater Devices, 2021, 6: 551–559

134 Wang W, Zhang H, Chen Y, *et al.* Efficient degradation of tetracycline *via* coupling of photocatalysis and photo-fenton processes over a 2D/2D α-Fe_2O_3/g-C_3N_4 S-scheme heterojunction catalyst. Acta Physico Chim Sin, 2022, 0: 2201008–0

135 Zhang C, Jia M, Xu Z, *et al.* Constructing 2D/2D N-ZnO/g-C_3N_4 S-scheme heterojunction: Efficient photocatalytic performance for norfloxacin degradation. Chem Eng J, 2022, 430: 132652

136 Van KN, Huu HT, Nguyen Thi VN, *et al.* Facile construction of S-scheme SnO_2/g-C_3N_4 photocatalyst for improved photoactivity. Chemosphere, 2022, 289: 133120

137 Tang R, Gong D, Deng Y, *et al.* π-π Stacked step-scheme PDI/g-C_3N_4/TiO_2@Ti_3C_2 photocatalyst with enhanced visible photocatalytic degradation towards atrazine *via* peroxymonosulfate activation. Chem Eng J, 2022, 427: 131809

138 Van Pham V, Truong TK, Le HV, *et al.* Enhancing green product generation of photocatalytic NO oxidation: A case of WO_3 nanoplate/g-C_3N_4 S-scheme heterojunction. Langmuir, 2022, 38: 4138–4146

139 Li X, Fang G, Tian Q, *et al.* Crystal regulation of $BiVO_4$ for efficient photocatalytic degradation in g-C_3N_4/$BiVO_4$ heterojunction. Appl Surf Sci, 2022, 584: 152642

140 Luo J, Han H, Wu J, *et al.* Excellent photocatalytic activity of MoO_3-adorned g-C_3N_4 systems: Construction of S-scheme heterojunction. Appl Surf Sci, 2022, 604: 154512

141 Guo Y, Li M, Huang X, *et al.* S-scheme g-C_3N_4/TiO_2/CFs heterojunction composites with multi-dimensional through-holes and enhanced visible-light photocatalytic activity. Ceramics Int, 2022, 48: 8196–8208

142 Chen N, Jia X, He H, *et al.* Promoting photocarriers separation in S-scheme system with Ni_2P electron bridge: The case study of BiOBr/Ni_2P/g-C_3N_4. Chin J Catal, 2022, 43: 276–287

143 He R, Ou S, Liu Y, *et al. In situ* fabrication of Bi_2Se_3/g-C_3N_4 S-scheme photocatalyst with improved photocatalytic activity. Chin J Catal, 2022, 43: 370–378

144 Ni S, Fu Z, Li L, *et al.* Step-scheme heterojunction g-C_3N_4/TiO_2 for efficient photocatalytic degradation of tetracycline hydrochloride under UV light. Colloids Surfs A-Physicochem Eng Aspects, 2022, 649: 129475

145 Li Y, Wang G, Zhang H, *et al.* Hierarchical flower-like 0D/3D g-C_3N_4/TiO_2 S-scheme heterojunction with enhanced photocatalytic activity. Colloids Surfs A-Physicochem Eng Aspects, 2022, 646: 128942

146 Lun Y, Hu S, Chen F, *et al.* Highly enhanced photocatalytic property dominantly owing to the synergic effects of much negative Ecb and S-scheme heterojunctions in composite g-C_3N_4/Mo-doped WO_3. Colloids Surfs A-Physicochem Eng Aspects, 2022, 642: 128682

147 Deng X, Wang D, Li H, *et al.* Boosting interfacial charge separation and photocatalytic activity of 2D/2D g-C_3N_4/$ZnIn_2S_4$ S-scheme heterojunction under visible light irradiation. J Alloys Compd, 2022, 894: 162209

148 Feng X, Li X, Su B, *et al.* Hydrothermal construction of flower-like g-C_3N_4/NiZnAl-LDH S-scheme heterojunction with oxygen vacancies for enhanced visible-light triggered photocatalytic performance. J Alloys Compd, 2022, 922: 166098

149 Elavarasan N, Vignesh S, Srinivasan M, *et al.* Synergistic S-Scheme mechanism insights of g-C_3N_4 and rGO combined ZnO-Ag heterostructure nanocomposite for efficient photocatalytic and anticancer activities. J Alloys Compd, 2022, 906: 164255

150 Yuan F, Zheng Y, Gao D, *et al.* Facile assembly and enhanced visible-light-driven photocatalytic activity of S-scheme BiOBr/g-C_3N_4 heterojunction for degrading xanthate in wastewater. J Mol Liquids, 2022, 366: 120279

151 Nguyen Thi TH, Huu HT, Phi HN, *et al.* A facile synthesis of SnS_2/g-C_3N_4 S-scheme heterojunction photocatalyst with enhanced photocatalytic performance. J Sci-Adv Mater Devices, 2022, 7: 100402

152 Gou L, Wang WQ, Liu EZ, *et al.* Fabrication of MOF-derived $CoTiO_3$/g-C_3N_4 S-scheme heterojunction for photocatalyst wastewater treat-

ment. J Alloys Compd, 2022, 918: 165698
153 Xu Q, Wang P, Wang Z, *et al.* Aerosol self-assembly synthesis of g-C_3N_4/MXene/Ag_3PO_4 heterostructure for enhanced photocatalytic degradation of tetracycline hydrochloride. Colloids Surfs A-Physicochem Eng Aspects, 2022, 648: 129392
154 Tang H, Li R, Fan X, *et al.* A novel S-scheme heterojunction in spent battery-derived $ZnFe_2O_4$/g-C_3N_4 photocatalyst for enhancing peroxymonosulfate activation and visible light degradation of organic pollutant. J Environ Chem Eng, 2022, 10: 107797
155 Zhou L, Li Y, Zhang Y, *et al.* A 0D/2D $Bi_4V_2O_{11}$/g-C_3N_4 S-scheme heterojunction with rapid interfacial charges migration for photocatalytic antibiotic degradation. Acta Physico Chim Sin, 2022, 0: 2112027–0
156 Zhang B, Hu X, Liu E, *et al.* Novel S-scheme 2D/2D BiOBr/g-C_3N_4 heterojunctions with enhanced photocatalytic activity. Chin J Catal, 2021, 42: 1519–1529
157 Dai Z, Zhen Y, Sun Y, *et al.* $ZnFe_2O_4$/g-C_3N_4 S-scheme photocatalyst with enhanced adsorption and photocatalytic activity for uranium(VI) removal. Chem Eng J, 2021, 415: 129002
158 Lian X, Xue W, Dong S, *et al.* Construction of S-scheme Bi_2WO_6/g-C_3N_4 heterostructure nanosheets with enhanced visible-light photocatalytic degradation for ammonium dinitramide. J Hazard Mater, 2021, 412: 125217
159 Wang J, Wang G, Cheng B, *et al.* Sulfur-doped g-C_3N_4/TiO_2 S-scheme heterojunction photocatalyst for Congo red photodegradation. Chin J Catal, 2021, 42: 56–68
160 Qin D, Xia Y, Li Q, *et al.* One-pot calcination synthesis of $Cd_{0.5}Zn_{0.5}S$/g-C_3N_4 photocatalyst with a step-scheme heterojunction structure. J Mater Sci Tech, 2020, 56: 206–215
161 Pan T, Chen D, Xu W, *et al.* Anionic polyacrylamide-assisted construction of thin 2D-2D WO_3/g-C_3N_4 Step-scheme heterojunction for enhanced tetracycline degradation under visible light irradiation. J Hazard Mater, 2020, 393: 122366
162 Li Q, Zhao W, Zhai Z, *et al.* 2D/2D Bi_2MoO_6/g-C_3N_4 S-scheme heterojunction photocatalyst with enhanced visible-light activity by Au loading. J Mater Sci Tech, 2020, 56: 216–226
163 Vijayakumar TP, Benoy MD, Duraimurugan J, *et al.* Investigation on photocatalytic activity of g-C_3N_4 decorated α-Fe_2O_3 nanostructure synthesized by hydrothermal method for the visible-light assisted degradation of organic pollutant. Diamond Relat Mater, 2022, 125: 109021
164 He R, Xu D, Li X. Floatable S-scheme photocatalyst for H_2O_2 production and organic synthesis. J Mater Sci Tech, 2023, 138: 256–258
165 Phan PDM, Nguyen DV, Anh NH, *et al.* S-scheme heterostructured CdS/g-C_3N_4 nanocatalysts for piezo-photocatalytic synthesis of H_2O_2. ACS Appl Nano Mater, 2023, 6: 16702–16715
166 Wei LW, Liu SH, Wang HP. Visible-light photocatalytic CO_2-to-CO and H_2 O-to-H_2O_2 by g-C_3N_4/Cu_2 O–Pd S-scheme heterojunctions. ACS Appl Mater Interfaces, 2023, 15: 25473–25483
167 Xia Y, Zhu B, Qin X, *et al.* Zinc porphyrin/g-C_3N_4 S-scheme photocatalyst for efficient H_2O_2 production. Chem Eng J, 2023, 467: 143528
168 Fang W, Yao S, Wang L, *et al.* Enhanced photocatalytic overall water splitting via hollow structure Pt/g-C_3N_4/BiOBr photocatalyst with S-scheme heterojunction. J Alloys Compd, 2022, 891: 162081
169 Das KK, Mansingh S, Mohanty R, *et al.* 0D-2D Fe_2O_3/Boron-doped g-C_3N_4 S-scheme exciton engineering for photocatalytic H_2O_2 production and photo-fenton recalcitrant-pollutant detoxification: Kinetics, influencing factors, and mechanism. J Phys Chem C, 2023, 127: 22–40
170 Jiang Z, Long Q, Cheng B, *et al.* 3D ordered macroporous sulfur-doped g-C_3N_4/TiO_2 S-scheme photocatalysts for efficient H_2O_2 production in pure water. J Mater Sci Tech, 2023, 162: 1–10
171 Wang Y, He Y, Chi Y, *et al.* Construction of S-scheme p-n heterojunction between protonated g-C_3N_4 and α-MnS nanosphere for photocatalytic H_2O_2 production and *in situ* degradation of oxytetracycline. J Environ Chem Eng, 2023, 11: 109968
172 Zan Z, Li X, Gao X, *et al.* 0D/2D carbon nitride quantum dots (CNQDs)/BiOBr S-scheme heterojunction for robust photocatalytic degradation and H_2O_2 production. Acta Physico Chim Sin, 2022, 0: 2209016
173 Li Z, Shen D, Hu X, *et al.* An S-scheme NH_2-MIL-101(Fe)@MCN/Bi_2O_3 heterojunction photocatalyst for the degradation of tetracycline and production of H_2O_2. Chemosphere, 2023, 343: 140234
174 Zhang X, Yu J, Macyk W, *et al.* C_3N_4/PDA S-scheme heterojunction with enhanced photocatalytic H_2O_2 production performance and its mechanism. Adv Sustain Syst, 2023, 7: 2200113
175 Li D, Liu Y, Xu D, *et al.* Construction of g-C_3N_4 nanotube/Ag_3PO_4 S-scheme heterojunction for enhanced photocatalytic oxygen generation. Ceramics Int, 2022, 48: 2169–2176
176 Mousavi M, Bonakdar A, Parsaei-Khomami A, *et al.* Visible-light-driven g-C_3N_4/$AgBiS_2$ S-scheme photocatalyst for N_2 fixation and rhodamine B degradation. J Phys Chem Solids, 2023, 179: 111376
177 Sayed M, Xu F, Kuang P, *et al.* Sustained CO_2-photoreduction activity and high selectivity over Mn, C-codoped ZnO core-triple shell hollow spheres. Nat Commun, 2021, 12: 4936
178 Wang L, Yu J. Photocatalytic phosphine-mediated water activation generates hydrogen atom radicals for transfer hydrogenation of closed-shell π systems. Sci China Mater, 2023, 66: 4133–4134
179 Zhu B, Sun J, Zhao Y, *et al.* Construction of 2D S-scheme heterojunction photocatalyst. Adv Mater, 2023, 2310600
180 Fang X, Tang Y, Ma YJ, *et al.* Ultralong-lived triplet excitons of room-temperature phosphorescent carbon dots located on g-C_3N_4 to boost photocatalysis. Sci China Mater, 2023, 66: 664–671
181 Dong J, Gong Z, Chen Y, *et al.* Organic microstructure-induced hierarchically porous g-C_3N_4 photocatalyst. Sci China Mater, 2023, 66: 3176–3188
182 Wang Y, Si W, Tan H, *et al.* Integrated molten and vapor condensation of polymeric carbon nitride photoelectrode towards efficient water splitting. Sci China Mater, 2023, 66: 623–633
183 Luo C, Long Q, Cheng B, *et al.* A DFT study on S-scheme heterojunction consisting of Pt single atom loaded G-C_3N_4 and BiOCl for photocatalytic CO_2 reduction. Acta Physico Chim Sin, 2023, 39: 2212026

Acknowledgements This work was supported by the National Natural Science Foundation of China (22302061 and 22075072), Hubei Provincial Natural Science Foundation of China (2022CFC060), and the Research Project of Hubei Provincial Department of Education (Q20212502).

Author contributions Wu X provided the overall concept, and wrote and revised the manuscript; Tan L and Chen G prepared the figures and tables; Kang J downloaded and organized the literature; Wang G wrote and revised the manuscript. All authors contributed to the general discussion.

Conflict of interest The authors declare no conflict of interest.

Xinhe Wu received his BS and MS degrees from Hubei Normal University and Wuhan University of Technology, respectively, and his PhD degree in materials science and engineering in 2021 from Wuhan University of Technology. In 2023, he became an associate professor at Hubei Normal University. Moreover, he was selected into the Chutian Scholars Talent Program of Hubei Province. His scientific interests are in semiconductor photocatalysis such as photocatalytic hydrogen production, CO_2 reduction to hydrocarbon fuels, and the degradation of antibiotics.

Guohong Wang received his BS and MS degrees in chemical technology from East China University of Science and Technology and Wuhan University of Science and Technology, respectively, and his PhD degree in materials physics and chemistry in 2008 from Wuhan University of Technology. In 2013, he became a professor at Hubei Normal University. His current research interests include semiconductor photocatalysis, photocatalytic hydrogen production, and CO_2 reduction to hydrocarbon fuels.

g-C_3N_4基S型异质结光催化剂

吴新鹤*, 谭丽红, 陈郭强, 康佳乐, 王国宏*

摘要 随着工业化的蓬勃发展, 能源短缺和环境污染日益严重, 威胁到人类的生存. 光催化技术因其诸多突出优点和广泛的应用前景被认为是解决能源和环境危机最有前途的技术之一. 在众多光催化剂中, 石墨氮化碳(g-C_3N_4)以其独特的电子结构、较高的热稳定性和突出的光电活性, 在清洁燃料生产和环境净化领域得到广泛应用. 然而, 单组分g-C_3N_4与其他光催化剂一样, 不可能同时拥有高的太阳能利用效率和强氧化还原能力的光生电荷, 导致其光催化效率较低. 幸运的是, g-C_3N_4与另一半导体构建异质结可以同时克服太阳能利用效率低、载流子重组快、氧化还原能力弱的缺点, 从而显著提高其光催化性能. 鉴于目前g-C_3N_4基S型异质结的广泛研究, 本文对g-C_3N_4基S型异质结研究背景、概念提出、基本理论、设计制备、表征方法等方面的最新研究进展进行了较全面的综述. 此外, 通过实例讨论和列表比较详细讨论了g-C_3N_4基S型异质结的各种应用, 包括光催化制H_2、还原CO_2、降解污染物、生产H_2O_2. 最后, 总结了g-C_3N_4基S型异质结当前的研究进展和不足, 并对未来的研究方向进行了展望.

